Reprints

RSC Advances

PAPER

Cite this: *RSC Adv.*, 2016, **6**, 83146

Fe_3O_4–Mn_3O_4 nanocomposites with moderate magnetism for *in vitro* cytotoxicity studies on macrophages†

Hasimur Rahaman,[a] Anupam Nath,[b] Rimi Paul,[a] Mahuya Sengupta[b] and Sujit Kumar Ghosh*[a]

Received 8th July 2016
Accepted 24th August 2016

DOI: 10.1039/c6ra17493k

www.rsc.org/advances

Dual magnetic iron oxide/manganese oxide nanocomposites have been synthesised by alkaline hydrolysis of a manganese precursor in the presence of preformed polyethylene glycol (PEG)-stabilised magnetite (Fe_3O_4) nanoparticles. The formation of the nanocomposites has been characterised by absorption spectroscopy, Fourier transform infrared spectroscopy, transmission electron microscopy, high resolution transmission electron microscopy, dynamic light scattering, selected area electron diffraction patterns, energy dispersive X-ray analysis, elemental mapping, X-ray diffraction patterns, Raman spectroscopy, thermogravimetric analysis and vibrating sample magnetometry. It has been shown that the synthesised Fe_3O_4–Mn_3O_4 nanocomposites exhibit reduced magnetism compared to the superparamagnetic Fe_3O_4 nanoparticles. The moderate magnetism of the Fe_3O_4–Mn_3O_4 nanocomposites offers a viable platform for *in vitro* cytotoxicity studies on macrophages.

1. Introduction

The integration of nanotechnology with molecular biology has emerged as nanobiotechnology that has pioneered exciting opportunities for discovering new materials, processes, and phenomena.[1] At the present age of human civilisation, due to increased stress conditions, the mind and body are, significantly, making an impact on the immune system that is responsible for the etiologic as well as pathologic mechanisms of various diseases.[2] It is, now, well established from animal studies that macrophages play an important role in the defence mechanism against host infection by innate and acquired immunity.[3] Macrophages are robust cells, known for their capability to kill pathogens or kill altered self-cells, *viz.*, tumor cells or virus infected cells or trigger lymphocytes to produce antibodies during the development of specific immunity and also increase the phagocytic activity and inflammatory responses in eliminating foreign matter.[3] In the process of phagocytosis, the macrophages produce cytokines, reactive oxygen species (ROS) and reactive nitrogen species (RNS) that are involved in the destruction of pathogens. To overcome the immunosupression and immunodepression that would hamper the resistivity against pathogens, cell viability and cytotoxicity assays are used for screening of certain chemicals that are able to destroy living cells. Based on these perspectives, the ability to accurately measure cytotoxicity is indispensable in identifying compounds that might pose certain health risks in humans and in the process of developing therapeutic anti-cancer drugs.[4]

Magnetic nanoparticles have engendered potential applications in a myriad of biological events, such as, magnetic bioseparation and biosensing, medical diagnosis and therapy, targeted drug delivery and biological labels.[5–7] Amongst the lexicon of magnetic nanoparticles, the superparamagnetism of magnetite along with low toxicity and excellent biocompatibility have been fascinated in biology and medicine, including, magnetohyperthermia,[8,9] diffusion through blood–brain barrier under magnetic field,[10] simultaneous magnetic resonance imaging and chemotherapy of ovarian cancer[11] *etc.* Among the series of manganese oxides available in various oxidation states of manganese(II, III, IV), hausmannite (Mn_3O_4) has been utilised as a platform for targeted magnetic resonance, fluorescence imaging of cancer cells,[12] as an intracellular drug delivery carrier[13] and so on. However, it has been experienced that the iron oxide nanoparticles synthesised as colloidal dispersion are highly magnetic and hydrophobic in nature that render their inherent tendency to agglomerate and limit their utility in numerous biomedical applications.[14] To impart stability and ensure nontoxicity under physiological conditions, researchers have often adopted the concept of molecular functionalisation with judiciously selected proper ligands, which ideally should have a high affinity for the iron oxide core, be nonimmunogenic and nonantigenic and prevent opsonisation by plasma

[a]*Department of Chemistry, Assam University, Silchar-788011, India. E-mail: sujit.kumar.ghosh@aus.ac.in*

[b]*Department of Biotechnology, Assam University, Silchar-788011, India*

† Electronic supplementary information (ESI) available: Absorption spectra, Raman scattering spectrum and thermogravimetric analysis. See DOI: 10.1039/c6ra17493k

proteins.[6,15] On the other hand, the conjugation of magnetic nanoparticles with quantum dots or metallic components produces nanocomposites with enhanced dispersity and provides a platform for improved medical imaging and controlled drug delivery, respectively.[16] As the third avenue to these two well-reputed roadmaps, the coupling of superparamagnetic Fe_3O_4 with relatively weak magnetic species could pave an effective strategy to avoid the tendency to agglomeration in colloidal dispersion. Magnetic iron oxide/manganese oxide nanocomposites have been found to possess potential applications in converting from superparamagnetic to antiferromagnetic materials,[17] environmental cleaning,[18] degradation of dye pollutants,[19] water oxidation catalysts[20] and magnetic resonance imaging of cancer cells[21] and so on. In this article, we demonstrate that reduced magnetism through the formation of Fe_3O_4–Mn_3O_4 nanocomposites could offer a viable platform for *in vitro* cytotoxicity determination on splenic macrophages in cell culture of mice. The advantages of maneuvering of Fe_3O_4–Mn_3O_4 nanocomposites are three folds: first, moderate magnetism to ensure good water dispersibility, colloidal stability and non-toxicity under physiological conditions; second, cytocompatibility of the average size distribution of the particles and third, benign and cost-effective synthetic strategy.

2. Experimental

2.1 Reagents and instruments

All the reagents used were of analytical grade reagent. Ferric chloride hexahydrate ($FeCl_3 \cdot 6H_2O$), ammonium ferrous sulphate hexahydrate [$(NH_4)_2Fe(SO_4)_2 \cdot 6H_2O$], manganese acetate tetrahydrate [$Mn(OOCCH_3)_2 \cdot 4H_2O$], Histopaque 1077, 3-(4,5-dimethylazol-2-yl)-2,5-diphenyl-tetrazolium bromide (MTT) were purchased from Sigma Aldrich and used as received. Other chemicals, PEG-13 (BroadPharm, San Diego, USA), nitroblue tetrazolium (NBT) (Sisco Research Laboratories, India), sulfanilamide (Himedia), *o*-phenylenediamine (Himedia), naphthylethylenediamine dihydrochloride (S. D. Fine Chemicals, India) and ammonium hydroxide (S. D. Fine Chemicals, India) were used without further purification. Animals were housed, handled and euthanised as per the regulations of Institutional Animal Ethics Committee, Assam University, Silchar. All animals were given standard rodent food and water *ad libitum*. All experiments were approved by Assam University Ethics Committee, Assam Universuty, Silchar (IEC/AUS/B/2013-015 dated 27-11-2013).

Absorption spectra of the samples were recorded in the solid state in a Perkin-Elmer Lambda 750 UV-vis-NIR digital spectrophotometer. Transmission electron microscopy (TEM) was carried out on a Zeiss CEM 902 microscope with a magnification of 200 kV. Samples were prepared by placing a drop of solution on a carbon coated copper grid. High resolution transmission electron micrograph (HRTEM) and selected area electron diffraction (SAED) pattern were obtained using the same instrument. Dynamic light scattering (DLS) studies were performed using a Malvern Zetasizer Nano ZS instrument after filtering the sample solution with a millipore syringe filter (0.2 mm pore size). Energy dispersive X-ray (EDX) analysis and elemental mapping were performed by Bruker's QUANTAX microanalysis system. Fourier transform infrared (FTIR) spectra were recorded in the form of pressed KBr pallets in the range (400–4000 cm^{-1}) in Shimadzu-FTIR Prestige-21 spectrophotometer. The powder X-ray diffraction patterns were obtained using a D8 ADVANCE BROKERaxs X-ray Diffractometer with CuK_α radiation ($\lambda = 1.4506$ Å); data were collected at a scan rate of 0.5° min^{-1} in the range of 10–80°. Raman scattering measurements were carried out on silicon substrate in backscattering geometry using a fiber-coupled micro-Raman spectrometer equipped with 488 nm (2.55 eV) of 5 mW air cooled Ar^+ laser as the excitation light source, a spectrometer (model TRIAX550, JY) and a CCD detector. Thermogravimetric analysis was carried out on a PerkinElmer STA 6000 with the sample amount of 10 mg. The measurements were performed under nitrogen with heating from 30–800 °C (rate: 10 °C min^{-1}) and then, maintained at 800 °C for half an hour. Before TGA measurements, the samples were dried overnight in vacuum oven at 50 °C. Magnetism of the nanostructured materials was measured at room temperature with a vibrating-sample magnetometer (Quantum Designed Physical Property Measurement System) in the presence of magnetic field in the range of ±15 kOe. Samples, in powder form, were immobilised in an epoxy resin to prevent any movement of the nanoparticles/nanocomposites during the measurements. Splenic macrophages were isolated from spleen tissue homogenate by density gradient centrifugation using Histopaque 1077 for characterisation of the biological events. Absorption spectra for the determination of cell cytotoxicity were measured in a PerkinElmer Lambda 750 spectrometer using 1 cm quartz cuvette at room temperature.

2.2 Synthesis of Fe_3O_4 NPs and Fe_3O_4–Mn_3O_4 NCs

Synthesis of Fe_3O_4 nanoparticles. Polyethylene glycol-stabilised (PEG with hydroxyl end groups has been used, named PEG-13) iron oxide nanoparticles have been synthesised by mixing 1 : 2 molar ratio of Fe^{2+} : Fe^{3+} by following the method reported by Gillich *et al.*[22] In a typical synthesis, 1.99 g $(NH_4)_2Fe(SO_4)_2 \cdot 6H_2O$ and 5.41 g $FeCl_3 \cdot 6H_2O$ were dissolved in 50 mL distilled water in a beaker. In a separate beaker, an aqueous NH_4OH (30% w/w) solution was prepared. After that, polyethylene glycol (18.6 g) was added at a ratio of M : L = 1 : 10 (9.3 g each) to both the above solutions to get precursor solutions I and II, respectively. Then, precursor solution II was added to solution I dropwise under stirring condition at 40 °C. Just after mixing the solutions, colour of the solution changes from light brown to black indicating the formation of Fe_3O_4 nanoparticles. The stirring was continued for another 45 min. The precipitate so obtained was washed thrice by centrifugation at 1000 rpm for 30 min and redispersion in distilled water. Finally, the as-obtained precipitate was dispersed in distilled water and stored in the vacuum desiccator.

Synthesis of Fe_3O_4–Mn_3O_4 nanocomposites. Dual magnetic metal oxide nanocomposites have been synthesised by alkaline hydrolysis of manganese precursor in the presence of as-synthesised Fe_3O_4 nanoparticles. In a typical synthesis, 1.0 mL aqueous dispersion of as-synthesised Fe_3O_4 nanoparticles (0.01

mmol) was added to an aqueous solution containing 0.1 mmol of $Mn(ac)_2 \cdot 4H_2O$ so as to maintain the final volume to 25 mL in a double-necked round bottom flask. The faint yellow colour reaction mixture was stirred for 30 min at room temperature and subsequently, hydrolysed at 65 °C. Initially, when the temperature was reached to 50 °C, ammonium hydroxide solution (30%, 2.0 mL) was added dropwise and a distinct colour change from faint yellow to brownish red was seen. The heating and stirring was continued for another 90 min. After that, the reaction mixture was cooled down to room temperature and stirring was continued overnight. The brownish red colour dispersion so obtained was washed thrice by centrifugation at 1000 rpm for 15 min (to avoid the precipitation of individual components) and redispersion in distilled water. Finally, the as-obtained precipitate was dispersed in distilled water and stored in the vacuum desiccator.

2.3 *In vitro* cytotoxicity studies on the macrophages with Fe_3O_4–Mn_3O_4 nanocomposites

Now, *in vitro* cytotoxicity in the splenic macrophages was determined with the moderately magnetic Fe_3O_4–Mn_3O_4 nanocomposites in a dose variant manner following the protocol reported in the literature.[2–4] The nanocomposites were found to be, adequately, dispersed at the selected concentrations for, at least, 72 h that was sufficient to perform cell culture experiments.

Isolation of splenic macrophages from mice. Spleen tissue was collected from individual mice and it was homogenised in Alsever's solution using Frosted glass slide. This homogenate was poured on Histopaque 1077 in 1 : 1 ratio and performed density gradient centrifugation. After centrifugation at 1500 rpm for 30 min, splenic macrophages were isolated from interface.

Cell viability assay. In a typical experiment, 10^6 cells were seeded in 96 well tissue culture plate and were kept overnight in CO_2 incubator. Then, the cells were treated with different concentrations of Fe_3O_4–Mn_3O_4 nanocomposites (1.8×10^6 to 1.8×10^{13} particles per mL) for 24 h. At the end of NCs exposure, toxicity was measured by 3-(4,5-dimethylazol-2-yl)-2,5-diphenyl-tetrazolium bromide (MTT) assay. In control experiment, cells were followed without any NCs treatment. Then, the cell viability was measured depending on the enzymatic reduction of MTT, a yellow tetrazolium salt to purple formazan at 570 nm with reference wavelength of 630 nm using microplate reader (i-Spectra plus; Bio-Rad). A schematic presentation showing the conversion of MTT to formazan in the presence of microbial reductase is shown in Scheme 1. All the experiments have been repeated thrice and an average of three determinations has been taken. The cell viability has been shown in percentage comparison to control that has been considered as 100%. All the raw data obtained have been followed by calculation and validated with statistical tools, such as, ANOVA, SEM, mean and variance *etc.* The data has been presented in mean ± SEM format and the significance has been tested at $P < 0.05$.

Nitroblue tetrazolium reduction (NBT) assay. Nitroblue tetrazolium (NBT) assay was performed in order to get the quantitative estimation of superoxide present in different test samples. The formation of formazan by the reaction of superoxide in the samples with NBT supplied in presence of EDTA catalyst gives blue colour measurable in visible spectra, which indicates the amount of superoxide present in the sample and their alteration upon nanoparticle treatment. From the NBT assay, the concentration of NBT was calculated from the OD at 630 nm and the extent of ROS present was determined.

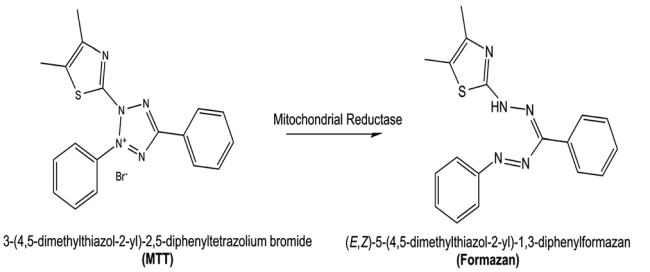

Scheme 1 Schematic presentation showing the conversion of MTT to formazan.

Myeloperoxidase (MPO) release assay. For the myeloperoxidase release assay, a volume of 200 μL of cell suspension from different groups was taken into microcentrifuge tubes and stimulated with lipopolysaccharide (LPS) (100 ng mL^{-1}) at 37 °C for 1 h and centrifuged at 13 000 rpm for 10 min. The supernatant, thus, obtained from different sets was recovered separately and kept at −20 °C until further use. The cell free supernatant was used for assay of the partial MPO release for different groups. The pallet that was recovered from the groups was lysed in 0.01% SDS and then, centrifuged again; the supernatant was recovered as before for total MPO release assay. Subsequently, 100 μL of cell free supernatant as well as from cell-lysates was allowed to react with 100 μL substrate buffer and kept at 37 °C for 20 min after which the reaction was stopped by adding 100 μL of 2.0 N H_2SO_4 and absorbance of the solution was measured at 492 nm.

Nitric oxide (NO) release assay. For nitric oxide release assay, a volume of 100 μL of macrophage cells were isolated from respective groups from 10^6 cells per mL dilution and then, suspended in DPBS-BSA. The cells were, then, stimulated with LPS (100 ng mL^{-1}) at 370 °C for 1 h and centrifuged at 13 000 rpm for 10 min. The cell free supernatants were transferred to separate microcentrifuge tubes for nitric oxide release assay. Then, 100 μL of Griess reagent was added and incubated at room temperature for 10 min. The absorbance of the solutions was measured in the UV-vis spectrophotometer at 550 nm and compared with a sodium nitrite standard curve.

3. Results and discussion

In this experiment, Fe_3O_4–Mn_3O_4 nanocomposites have been synthesised by alkaline hydrolysis of manganese precursor in the presence of preformed polyethylene glycol-stabilised Fe_3O_4 nanoparticles. The nanostructures have been examined by absorption spectroscopy, Fourier transform infrared (FTIR) spectroscopy, transmission electron microscopy (TEM), high

resolution transmission electron microscopy (HRTEM), dynamic light scattering (DLS), selected area electron diffraction (SAED) pattern, energy dispersive X-ray (EDX) analysis, elemental mapping, X-ray diffraction (XRD) pattern, Raman spectroscopy, thermogravimetric analysis (TGA) and vibrating sample magnetometry (VSM).

The morphology, composition and crystallinity of the Fe_3O_4 NPs and Fe_3O_4–Mn_3O_4 NCs are described in Fig. 1. Representative transmission electron micrographs of Fe_3O_4 (panel a) and Fe_3O_4–Mn_3O_4 (panel b) exhibit that the particles are spherical or nearly spherical with average diameter 8 ± 1 and 12 ± 2 nm, respectively. Inset in panel (b) shows that the number distribution hydrodynamic diameter of Fe_3O_4–Mn_3O_4 NCs is *ca.* 15 ± 5 nm. The small discrepancy in the particle size obtained from TEM and DLS measurements could be attributed to factors associated with the high vacuum conditions of TEM and the hydrodynamic and electrokinetic effects operative in DLS measurements.[23] Selected area electron diffraction pattern of the Fe_3O_4 nanoparticles (panel c) exhibits five diffraction rings of (220), (311), (420), (511) and (440) that confirm a typical magnetite crystalline structure.[24] Selected area electron diffraction pattern of the Fe_3O_4–Mn_3O_4 nanocomposites (panel d) is consistent with diffraction rings of magnetite as well as tetragonal Mn_3O_4 with strong ring patterns due to (101), (103) and (220) planes. The observation of distinct ring patterns in the nanocomposites implies that the presence of preformed magnetite favours the formation of an ordered and single phase of Mn_3O_4 in the nanocomposites. High resolution transmission electron micrograph (panel e) of Fe_3O_4–Mn_3O_4 nanocomposites displays two distinct lattice spacings of 0.254 nm resulting from a group of (111) planes of Fe_3O_4 (ref. 25) and 0.249 nm which corresponds to the distance between the (211) planes of the Mn_3O_4 (ref. 26) tetragonal crystal lattice. Elemental mapping of the nanocomposites (panel f) exhibits the appearance of the blue, green and red coloured micrographs revealing the presence of oxygen (O), manganese (Mn) and iron (Fe), respectively.

Further insights into the nanocomposites have been augmented from multiple control experiments. Absorption measurements and band gap determination (ESI 1†) of Fe_3O_4 NPs and Fe_3O_4–Mn_3O_4 NCs reveal the electronic interaction amongst the components in the nanocomposites.[27] Representative energy dispersive X-ray spectrum of Fe_3O_4–Mn_3O_4 nanocomposites (Fig. 2) reveals that the particles are composed of Fe, Mn and O elements. Fourier transform infrared spectra (Fig. 3) of the as-prepared of Fe_3O_4 NPs and Fe_3O_4–Mn_3O_4 NCs elucidate the presence of two bands at 512 and 619 cm^{-1} due to Mn–O and Fe–O vibrations, respectively, confirming the presence of both the species in the composites.[28] For the structural characterisation of synthesised materials, comparative powder X-ray diffraction patterns of Fe_3O_4 NPs and Fe_3O_4–Mn_3O_4 NCs are shown in Fig. 4. All diffraction peaks of trace a implying a crystalline structure can be indexed to the presence of inverse spinel structure of magnetite (JCPDS# 89-0691). Upon conjugation with the manganese oxide, the presence of all the diffraction peaks in trace b implying a crystalline structure can be indexed to the presence of inverse spinel structure of magnetite (JCPDS# 89-0691) and tetragonal hausmannite (JCPDS# 24-0734) with space groups F_{d3m} and $I4_{1/amd}$,

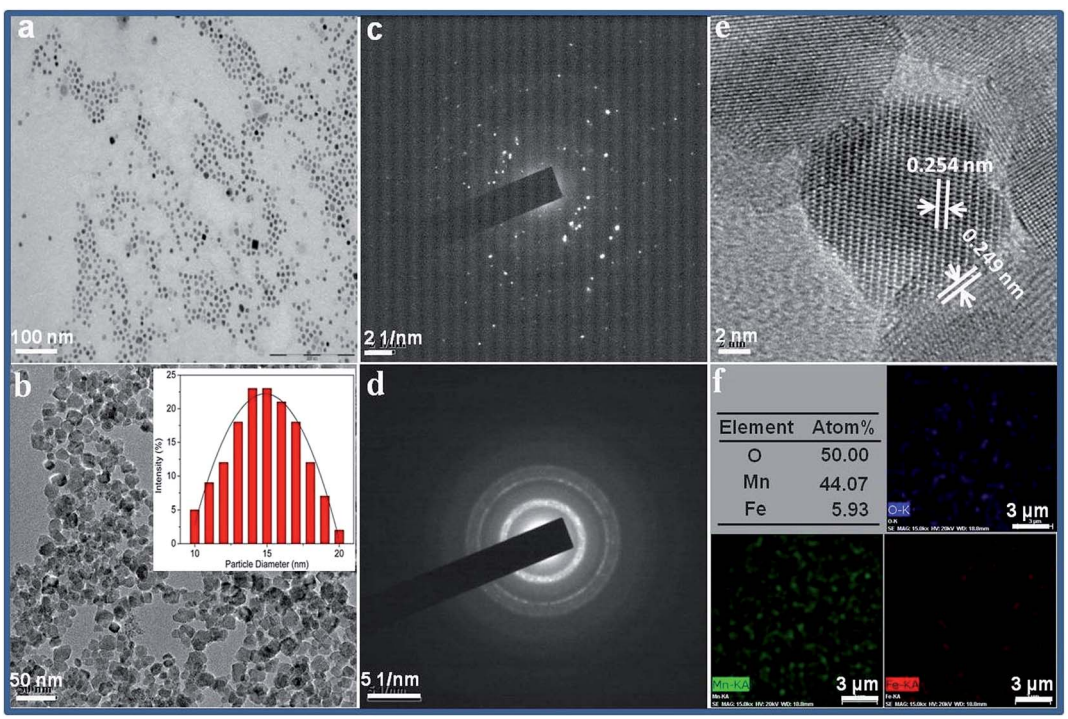

Fig. 1 (a and b) Representative transmission electron micrographs and (c and d) selected area electron diffraction patterns of Fe_3O_4 nanoparticles and Fe_3O_4–Mn_3O_4 nanocomposites, respectively; (e) high resolution transmission electron micrograph and (f) elemental mapping of Fe_3O_4–Mn_3O_4 nanocomposites. Inset in panel (b) shows the dynamic light scattering spectrum of the Fe_3O_4–Mn_3O_4 nanocomposites.

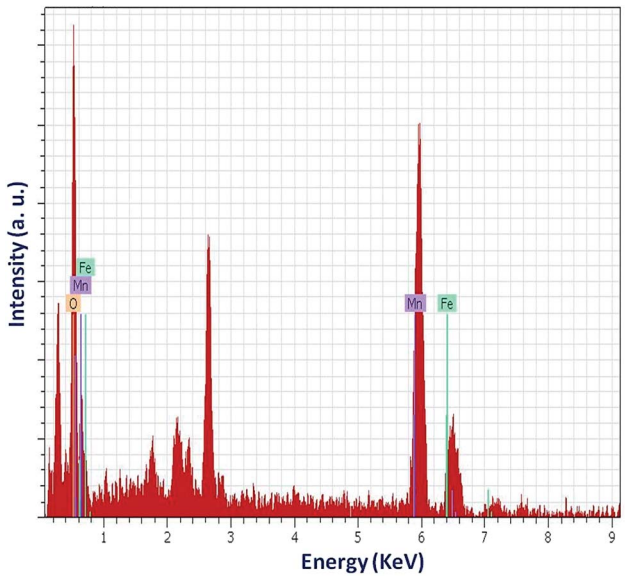

Fig. 2 Energy dispersive X-ray spectrum of Fe_3O_4–Mn_3O_4 nanocomposites.

respectively, which indicate that preformed magnetite favours the formation of an ordered and single phase Mn_3O_4 in the nanocomposites.[29] The room temperature Raman spectrum (ESI 2†) of Fe_3O_4–Mn_3O_4 nanocomposites shows that the peak positions are, substantially, shifted to that of the original positions which authenticates the formation of Fe_3O_4–Mn_3O_4 nanocomposites.[30,31] Thermogravimetric analysis (ESI 3†) of the as-dried powder sample shows two weight loss steps implying that the polyethylene glycol molecules employed for the stabilisation of Fe_3O_4 nanoparticles are, even, incorporated into the nanocomposites.[32]

The magnetic hysteresis curves of the synthesised Fe_3O_4 NPs and Fe_3O_4–Mn_3O_4 NCs over the range of $-15 < H < 15$ kOe at room temperature are presented in Fig. 5. It is seen that the both types of particles are superparamagnetic; the saturation magnetisation of Fe_3O_4 NPs and Fe_3O_4–Mn_3O_4 NCs are 24.97 and 14.26 emu g^{-1}, respectively. It is, thus, evident that the saturation magnetisation value of Fe_3O_4–Mn_3O_4 NCs is lower compared to that of the Fe_3O_4 NPs.[21] Inset shows the digital camera photograph of the response (for a time span of 30 min) of the Fe_3O_4 NPs and Fe_3O_4–Mn_3O_4 NCs in the presence of a bar magnet. Strong attraction of the Fe_3O_4 NPs than that of the Fe_3O_4–Mn_3O_4 NCs towards an external magnetic field reveals

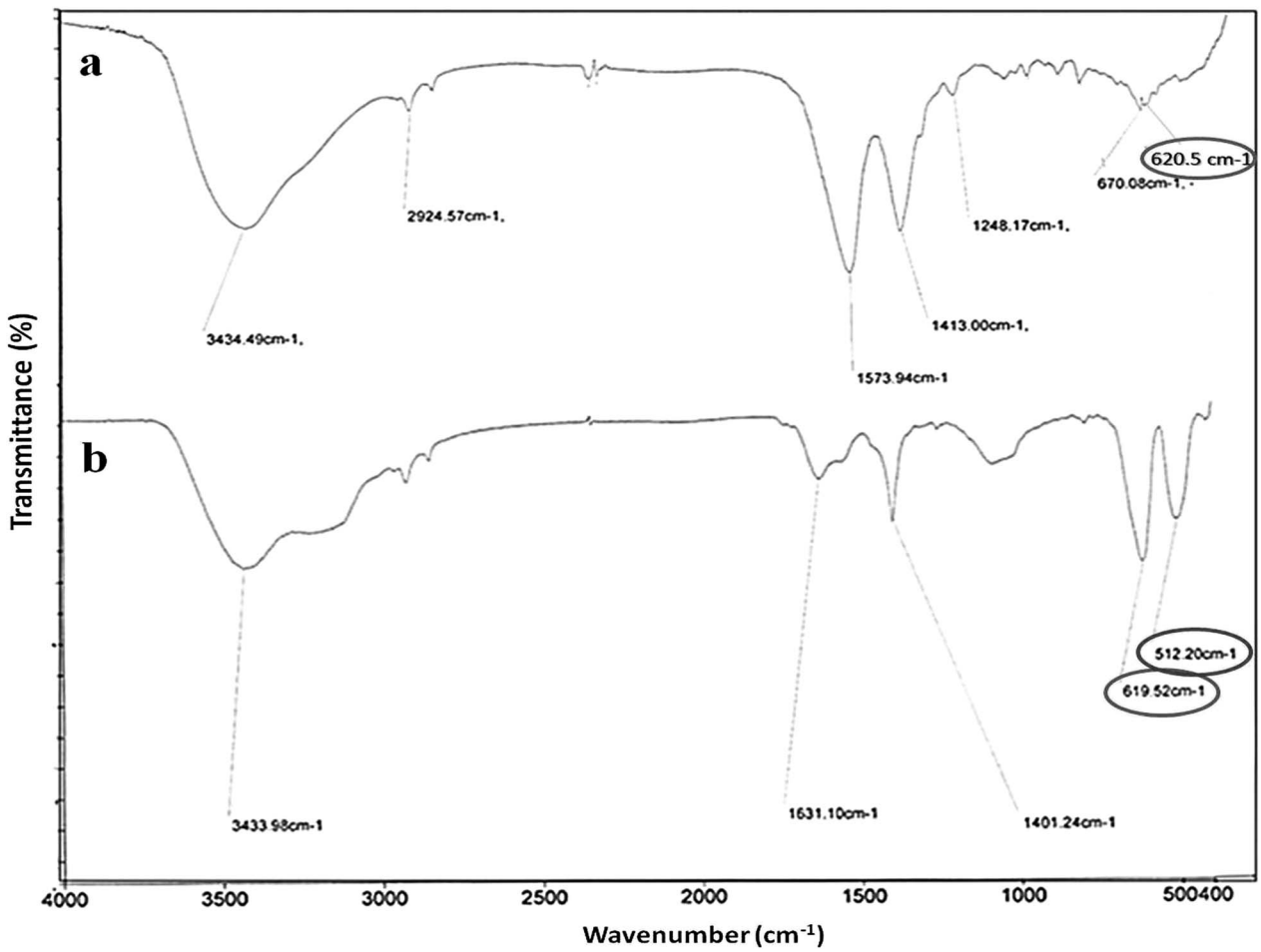

Fig. 3 Fourier transform infrared spectra of the as-prepared (a) Fe_3O_4 NPs and (b) Fe_3O_4–Mn_3O_4 NCs.

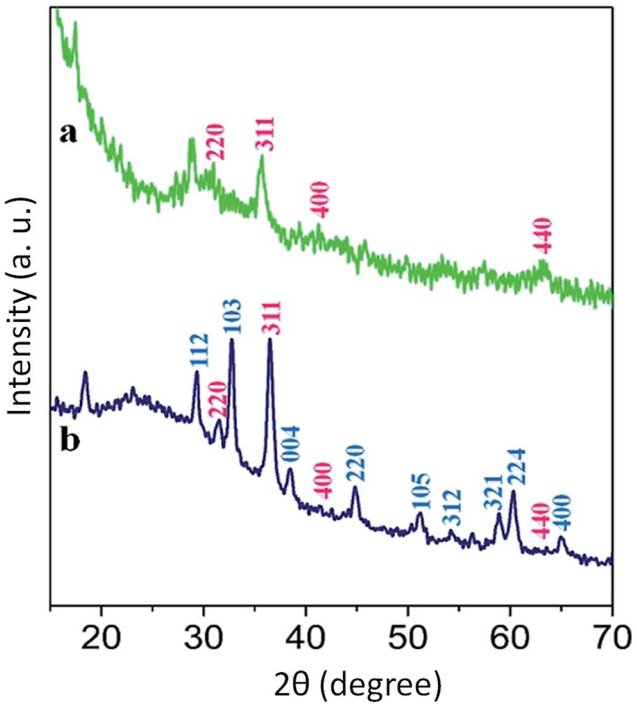

Fig. 4 X-ray diffraction patterns of (a) Fe_3O_4 NPs and (b) Fe_3O_4–Mn_3O_4 NCs.

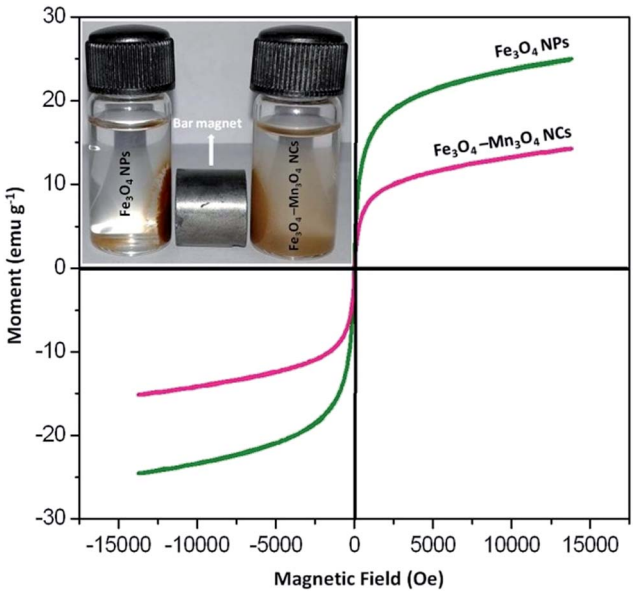

Fig. 5 Magnetic hysteresis curves of Fe_3O_4 NPs and Fe_3O_4–Mn_3O_4 NCs. Inset shows the digital camera photographs showing the response of the nanostructures in the presence of a magnetic bar.

that magnetism of the iron oxide particles are reduced upon conjugation with the Mn_3O_4 entities. The Fe_3O_4–Mn_3O_4 nanocomposites dispersion (right bottle), apparently, seems cloudy due to incomplete magnetic separation by the bar magnet. The decrease of the saturation magnetisation can, mainly, be attributed to the co-existence of weakly magnetic Mn_3O_4 in the composites. Therefore, the Fe_3O_4–Mn_3O_4 NCs with reduced magnetism may hold a great promise to be utilised as a nanoplatform for sensing of different biological species and processes.

Now, the moderately magnetic Fe_3O_4–Mn_3O_4 nanocomposites have been exploited to study *in vitro* cytotoxicity in the splenic macrophages. Assuming that the particles are nearly spherical and the density of Fe_3O_4 NPs and Fe_3O_4–Mn_3O_4 NCs as 5.17 and 12.87 g cm^{-3} (taking an average of the density of Fe_3O_4 and Mn_3O_4) respectively, the number of Fe_3O_4 and Fe_3O_4–Mn_3O_4 particles is *ca.* 2.16×10^{12} and 3.58×10^{11} mL^{-1}, respectively.[33,34] Proliferation of splenocytes was evaluated by 3-(4,5-dimethylthiazole-2-yl)-2,5-diphenyltetrazolium bromide (MTT) assay and immunomodulatory activity of the extract was examined on murine macrophage phagocytosis by nitrobluetetrazolium (NBT) dye reduction, myeloperoxidase (MPO) activity and nitric oxide (NO) estimation assay. Apart from assessing cytotoxic effect of the nanocomposites on splenic macrophages, we have also explored many other cell types, like, alveolar macrophages (macrophage cells of the lung) and Kupffer cells (liver macrophages) *etc.* The toxicity profiles of these cell types, including, those from the lungs, were not found to be significantly different from that of the splenic macrophages. Therefore, for the sake of simplicity, the cytotoxicity studies on splenic macrophages have been elaborated in detail.

Fig. 6 shows the histograms representing the *in vitro* cytotoxicity studies on the splenic macrophages with Fe_3O_4–Mn_3O_4 nanocomposites. A MTT assay has been used for assaying cell survival and proliferation based on the concentration of formazan generated which is directly proportional to the cell number.[35] It is seen that the cell viability displays a concentration-dependent effect (top left panel). Nanoparticle doses, as determined by MTT assay, have been fitted in a non-linear dose response curve (as shown in the inset) and it is seen that the IC_{50} (inhibitory concentration with 50% viability) of NCs is *ca.* 3.83×10^9 particles per mL of the solution. Therefore, for the rest of the studies, the effective concentration of the nanoparticles has been so chosen that it should fall below the value of IC_{50} and has been selected as 1.8×10^9 particles per mL of the solution. However, it is to be mentioned that while the IC_{50} value of the Fe_3O_4–Mn_3O_4 nanocomposites is 3.83×10^9 particles per mL of the solution, that of Fe_3O_4 and Mn_3O_4 nanoparticles is *ca.* 2.034×10^8 and 4.572×10^{11} particles per mL of the solution, respectively. The IC_{50} value of Fe_3O_4–Mn_3O_4 nanocomposites has been determined with the particles after washing by repeated centrifugation and re-dispersion so as to avoid the presence of unreacted Fe_3O_4 or Mn_3O_4 particles. These results imply that the cytotoxicity factor of the nanocomposites might, largely, be due to the inherent toxicity of the Fe_3O_4 rather than the Mn_3O_4 components.

The phagocytosis of the particles by macrophages is, usually, accompanied by a burst of oxidative metabolism allowing the generation of oxygen species which can be detected through reduction of nitroblue tetrazolium dye.[36] The higher reduction in NBT assay represented higher activity of the oxidase enzyme reflecting the stimulation of phagocytes in proportion to the foreign particles ingested. The oxidative burst, as evident from

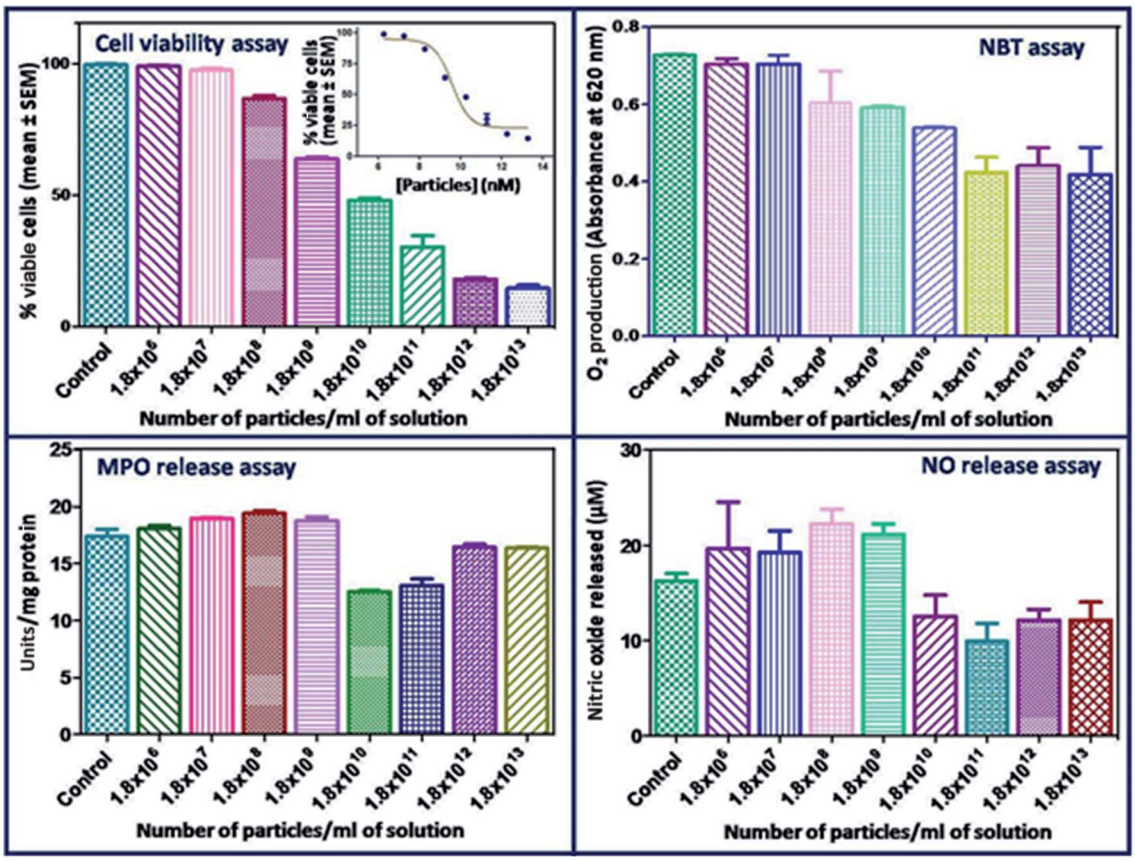

Fig. 6 Histograms showing the *in vitro* cytotoxicity studies on the splenic macrophages with Fe_3O_4–Mn_3O_4 nanocomposites. Inset in the top left panel shows the determination of IC_{50} of the cell viability assay.

the NBT reduction assay, shows a dose-dependent gradual increase (top right panel). However, the non-significant response for effective dose in NBT assay indicates that the cells are not in hypoxic condition and still maintain the normoxia which means that the cells do not experience the oxygen stress.

Again, myeloperoxidase is a heme protein secreted by neutrophils and macrophages which use the oxidizing potential of H_2O_2 to convert Cl^- into HOCl, a potent bactericidal agent.[37] A deficiency of MPO is indicative of an autosomal recessive genetic disorder featuring deficiency, either in quantity or of function of the enzyme. It is seen that the NCs did not show any visible effect on MPO release (bottom left panel) that could be because of the indigenous Fe of the enzyme itself. The non-significant level of MPO suggests that the particles are not imposing any oxidative stress.

Lastly, nitric oxide has been found to be the main effector molecule produced by macrophages by inducible nitric oxido-synthetase (iNOS) for cytotoxic activity and can be used as a quantitative index of macrophage activation.[38] It is seen that the NCs could determine the nitrosative stress on the splenic macrophages as revealed by the increase in NO release till 1.6×10^9 dose after which the NCs become cytotoxic. The significant level of NO release indicates that the particles generate reactive nitrogen species, largely, indicating the effect of NCs on the intracellular metabolic status in splenic macrophages.

4. Conclusions

In a nutshell, Fe_3O_4–Mn_3O_4 nanocomposites have been synthesised by alkaline hydrolysis of manganese precursor in the presence of preformed polyethylene glycol-stabilised Fe_3O_4 nanoparticles. It has been investigated that conjugation of weakly magnetic Mn_3O_4 with the superparamagnetic Fe_3O_4 nanoparticles renders the nanocomposites to be moderately magnetic that ensures good water dispersibility, colloidal stability and non-toxicity under physiological conditions. The integration of magnetism in multicomponent Fe_3O_4–Mn_3O_4 nanocomposites has been exploited for *in vitro* cytotoxicity determination on splenic macrophages of mice. The present study clearly demonstrates that moderately magnetic nanocomposites could act as viable substrates to measure the oxidative and nitrosative stress of the immune competent cells. Further studies can be elicited to study the effect of these nanocomposites *in vivo* experiments in living systems and their therapeutic potential could be adjudged in physiological environments.

Acknowledgements

We gratefully acknowledge financial support from DBT, New Delhi (Project No. BT/277/NE/TBP/2012). We are thankful to Dr Achintya Sinha, Bose Institute, Kolkata for providing facilities for Raman measurements.

References

1 M. De, P. S. Ghosh and V. M. Rotello, *Adv. Mater.*, 2008, **20**, 4225–4241.

2 A. K. Abbas, A. H. H. Lichtman and S. Pillai, in *Basic Immunology: Functions and Disorders of the Immune System*, Saunders, Wilmington, USA, 4th edn, 2012.

3 J. Sun, A. Siroy, R. K. Lokareddy, A. Speer, K. S. Doornbos, G. Cingolani and M. Niederweis, *Nat. Struct. Mol. Biol.*, 2015, **22**, 672–678.

4 G. W. Cox, Assay for Macrophage-Mediated Anti-Tumor Cytotoxicity, in *Current Protocols in Immunology*, John Wiley and Sons, New York, 2003.

5 J. Gao, H. Gu and B. Xu, *Acc. Chem. Res.*, 2009, **42**, 1097–1107.

6 S. Laurent, D. Forge, M. Port, A. Roch, C. Robic, L. V. Elst and R. N. Muller, *Chem. Rev.*, 2008, **108**, 2064–2110.

7 M. M. J. Modo and J. W. M. Bulté, in *Molecular and Cellular MR Imaging*, CRC Press, Boca Raton, FL, 2007.

8 L. M. Bauer, S. F. Situ, M. A. Griswold and A. C. S. Samia, *Nanoscale*, 2016, **8**, 12162–12169.

9 J. M. Orozco-Henao, D. F. Coral, D. Muraca, O. Moscoso-Londoño, P. Mendoza Zélis, M. B. Fernandez van Raap, S. K. Sharma, K. R. Pirota and M. Knobel, *J. Phys. Chem. C*, 2016, **120**, 12796–12809.

10 Y. Huang, B. Zhang, S. Xie, B. Yang, Q. Xu and J. Tan, *ACS Appl. Mater. Interfaces*, 2016, **8**, 11336–11341.

11 H. M. Vishwasrao, A. M. Master, Y. G. Seo, X. M. Liu, N. Pothayee, Z. Zhou, D. Yuan, M. D. Boska, T. K. Bronich, R. M. Davis, J. S. Riffle, M. Sokolsky-Papkov and A. V. Kabanov, *Chem. Mater.*, 2016, **28**, 3024–3040.

12 H. Yang, Y. Zhuang, H. Hu, X. Du, C. Zhang, X. Shi, H. Wu and S. Yang, *Adv. Funct. Mater.*, 2010, **20**, 1733–1741.

13 J. Shin, R. M. Anisur, M. K. Ko, G. H. Im, J. H. Lee and I. S. Lee, *Angew. Chem., Int. Ed.*, 2009, **48**, 321–324.

14 L. Zhang, W.-F. Dong and H.-B. Sun, *Nanoscale*, 2013, **5**, 7664–7684.

15 P. H. Mutin, G. Guerrero and A. Vioux, *J. Mater. Chem.*, 2005, **15**, 3761–3768.

16 J. Kim, J. E. Lee, S. H. Lee, J. H. Yu, J. H. Lee, T. G. Park and T. Hyeon, *Adv. Mater.*, 2008, **20**, 478–483.

17 J. Lai, K. V. P. M. Shafi, A. Ulman, K. Loos, N.-L. Yang, M.-H. Cui, T. Vogt, C. Estournés and D. C. Locke, *J. Phys. Chem. B*, 2004, **108**, 14876–14883.

18 C. Luo, Z. Tian, B. Yang, L. Zhang and S. Yan, *Chem. Eng. J.*, 2013, **234**, 256–265.

19 L. Zhang, J. Lian, L. Wu, Z. Duan, J. Jiang and L. Zhao, *Langmuir*, 2014, **30**, 7006–7013.

20 G. Elmaci, C. E. Frey, P. Kurz and B. Zümreoğlu-Karan, *Inorg. Chem.*, 2015, **54**, 2734–2741.

21 J. Li, Y. Hu, W. Sun, Y. Luo, X. Shi and M. Shen, *RSC Adv.*, 2016, **6**, 35295–35304.

22 T. Gillich, C. Acikgöz, L. Isa, A. D. Schlüter, N. D. Spencer and M. Textor, *ACS Nano*, 2013, **22**, 316–329.

23 U. Nobbmann and A. Morfesis, *Mater. Today*, 2009, **12**, 52–54.

24 R. M. Cornell and U. Schwertmann, in *The Iron Oxides*, VCH, Weinheim, 2nd edn, 2003.

25 C. Hui, C. Shen, T. Yang, L. Bao, J. Tian, H. Ding, C. Li and H.-J. Gao, *J. Phys. Chem. C*, 2008, **112**, 11336–11339.

26 C. Ray, S. Dutta, Y. Negishi and T. Pal, *Chem. Commun.*, 2016, **52**, 6095–6098.

27 J. Tang, M. Myers, K. A. Bosnick and L. E. Brus, *J. Phys. Chem. B*, 2003, **107**, 7501–7506.

28 W. Zhang, X. Li, R. Zou, H. Wu, H. Shi, S. Yu and Y. Liu, *Sci. Rep.*, 2015, **5**, 1–9.

29 R. E. Dinnebier and S. J. L. Billingue, in *Powder Diffraction Theory and Practice*, The Royal Society Chemistry, London, UK, 1st edn, 2008, p. 604.

30 C. M. Julien and M. Massot, *J. Phys.: Condens. Matter*, 2003, **15**, 3151–3162.

31 M. Kim, X. M. Chen, Y. I. Joe, E. Fradkin, P. Abbamonte and S. L. Cooper, *Phys. Rev. Lett.*, 2010, **104**, 136402.

32 H.-P. Cong and S.-H. Yu, *Adv. Funct. Mater.*, 2007, **17**, 1814–1820.

33 Y. Tang and W. Cheng, *Langmuir*, 2013, **29**, 3125–3132.

34 H. Rahaman, K. Barman, S. Jasimuddin and S. K. Ghosh, *RSC Adv.*, 2014, **4**, 41976–41981.

35 A. Mantovani, W. J. Ming, C. Balott, B. Abdeljalil and B. Bottazzi, *Biochim. Biophys. Acta*, 1986, **865**, 59–67.

36 S. Jayadev, in *NBT Assay: Bruce Weinberg Protocol*, Medical University of South Carolina, January 10, 1991.

37 J. W. Heinecke, W. Li, G. A. Francis and J. A. Goldstein, *J. Clin. Invest.*, 1993, **91**, 2866–2872.

38 A. M. Miles, *Methods Enzymol.*, 1996, **268**, 105–120.

RSC Advances

PAPER

Cite this: *RSC Adv.*, 2016, **6**, 4531

Soft-templated synthesis of Mn_3O_4 microdandelions for the degradation of alizarin red under visible light irradiation†

Hasimur Rahaman and Sujit Kumar Ghosh*

Received 5th December 2015
Accepted 23rd December 2015

DOI: 10.1039/c5ra25935e

www.rsc.org/advances

A facile wet chemical approach has been developed for the soft-templated synthesis of self-assembled Mn_3O_4 microdandelions through an effective dye/surfactant (*viz.*, fluorescein isothiocyanate–dextran 2000S/cetyltrimethylammonium bromide) interaction. Addition of FITC D-2000S to an aqueous solution of CTAB results in the formation of aggregates that act as soft templates for the formation of Mn_3O_4 microdandelions upon addition of a weak base, diethanolamine to manganese acetate as the precursor under mild refluxing conditions. The morphology of these hybrid materials has been characterised by UV-visible, Fourier transform infrared (FTIR) and energy dispersive X-ray (EDX) spectroscopy, high resolution transmission electron microscopy (HRTEM), scanning electron microscopy (SEM), X-ray diffraction (XRD) technique, selected area electron diffraction (SAED) pattern and thermogravimetric analysis (TGA). The surface area of the microdandelions has been determined by Brunauer–Emmett–Teller (BET) analysis. The Mn_3O_4 microdandelions, bearing high surface area, exhibit potential photocatalytic activity towards the degradation of dye, *viz.*, alizarin red under visible light irradiation under ambient conditions.

1. Introduction

In recent years, the fabrication of metal oxide superstructures has fascinated scientists for studying the physics of materials in two- or three-dimensions and their potential technological applications.[1–3] Self-organisation of metal oxide nanostructures provides extraordinary richness of morphological and physico-chemical diversity for emerging unprecedented architectures.[4–6] Manganese oxides are materials of considerable importance due to their interesting structural, electronic and magnetic properties that arise from their outstanding structural flexibility combined with novel physical and chemical properties.[7,8] Moreover, manganese oxides are ubiquitous in nature and environmental friendly that deserve their applications in catalysis, renewable energy, and environmental remediation.[9,10] Among the series of manganese oxides available in various oxidation states of manganese (II, III, IV), Mn_3O_4 (hausmannite) has been found to be an effective and inexpensive catalyst in versatile reactions.[11–17] The corresponding surface energy values of Mn_3O_4 (0.96 ± 0.08 J m^{-2}), Mn_2O_3 (1.29 ± 0.10 J m^{-2}), and MnO_2 (1.64 ± 0.10 J m^{-2}), suggest considerable thermodynamic stability of Mn_3O_4 over other oxidation states.[18] Moreover, Mn_3O_4 possess several special structural attributes:[19] (i) it shows semicovalent character in tetrahedral sites (Mn II occupancy with Mn–O distance of 1.812 Å) and in the apical bonds of octahedral sites (Mn III occupancy with Mn–O lengths of 2.386 Å); (ii) the remaining bonds of the octahedra display ionic character with a Mn–O length of 2.977 Å; and (iii) the observed distortion in the octahedra found in both phases can be explained by a Jahn–Teller effect due to the d^4 state of the Mn III atoms in high spin configuration. Bulk Mn_3O_4 is a p-type semiconductor with a wide direct band gap of 2.3 eV and is the stablest among all the manganese oxides possessing tetragonally distorted spinel structure.[20]

The removal of the non-biodegradable organic chemicals is a global ecological problem. Dyes are an important class of synthetic organic compounds which are commonly used in textile industries and therefore, are common industrial pollutants. However, due to the inherent stability of modern dyes, conventional biological treatment methods for industrial waste water are ineffective. Photocatalysis, where photons are used for catalytically activating chemical reactions on the surface of photosensitized catalysts, remains one of the leading hubs of research for harvesting the solar light.[21–23] The efficiency of a photocatalytic process, mostly, depends on the nature of photosensitized catalyst, suitable photon source for excitation, the substrate which can rapidly accept the photogenerated charge carriers and the spatial distance between the catalyst and substrate.[24] Typically, photocatalysts generate the charge carriers on excitation and under suitable conditions, these are transferred from the catalysts to the reaction medium, which in

Department of Chemistry, Assam University, Silchar-788011, India. E-mail: sujit.kumar.ghosh@aus.ac.in; Fax: +91-3842-270802; Tel: +91-3842-270848

† Electronic supplementary information (ESI) available: Comparative account of surface area. See DOI: 10.1039/c5ra25935e

turn initiate the chemical reaction.[25] Since the pioneering work of Fujishima and Honda in 1972, photocatalysis by semiconductor metal oxide particles has been proven to be a promising technology for alleviating the global environmental pollution.[26]

Alizarin red, an industrially important synthetic textile dye of anthraquinone family, is a widespread polluting dye, whose inexpensive and environmental friendly elimination from effluents is a serious challenge. Although, the chemical and electrochemical degradation of alizarin red have been carried out by immobilized 5,10,15,20-tetrakis(4-sulfonatophenyl)porphine-Mn(III) as a biomimetic peroxidase-like catalyst,[27] electro-Fenton process using a graphite-felt cathode,[28] hybrid gas–liquid dielectric barrier discharge,[29] the photochemical degradation of the dye has, mainly, be relied upon the advent of semiconductor nanocatalysts. While the visible light-driven photocatalytic degradation of alizarin red has been carried out using nanostructures of TiO_2,[30] Bi-doped TiO_2,[31] ZnO,[32] Ag-impregnated ZnO,[33] CdS,[34] TiO_2–In_2O_3 composites,[35] UV-light assisted degradation has been pursued by TiO_2,[36] nanometer TiO_2 film,[37] electrospun bismuth oxoiodide nano/microtectonic plate-like structures[38] *etc.* In addition, sonophotocatalytic degradation of the dye has also been experimented with TiO_2 nanostructures.[39] Therefore, it is revealed that the photocatalytic degradation of alizarin red has, mostly, been experimented with TiO_2 or ZnO nanostructures or their composites. Based on these perspectives, Mn_3O_4, bearing many special structural attributes[19,40] and with the possibility of designing high surface area hierarchical 3D nano/microstructures[41] could offer an alternative low-cost, earth abundant, semiconductor, heterovalent-Mn photocatalyst for the degradation of alizarin red under visible light illumination.

Several synthetic strategies have been adopted, so far, in the literature for the fabrication of size and shape-selective manganese oxide nanocrystals and their assemblies using different types of soft templates and their application in catalysis. Chen and group[42] have described the synthesis of octahedral Mn_3O_4 nanocrystals by soft-template of cetyltrimethylammoniumbromide/poly(*N*-vinyl-2-pyrrolidone) mixture and the crystallites have been found to act efficient catalysts for the degradation of methylene blue. Ahmed and co-workers[43] have reported the synthesis of nanosized Mn_3O_4 single crystals using polyol method and investigated their catalytic activity towards the decomposition of aqueous hydrogen peroxide and degradation of methylene blue at room temperature. Takada and colleagues[44] have illustrated microorganism-mediated synthesis of nano- and micro-architectural manganese oxides that catalyse the selective bromination of hydrocarbons under irradiation of fluorescent light. Huang and co-authors[45] have reported the synthesis of Mn_3O_4 nanoparticles and hexagonal nanoplates by a solvothermal oxidation process and these materials were found to be catalytically active towards oxidation of aldehydes. Hu and co-workers[46] have described the synthesis of well-dispersed ultrafine Mn_3O_4 nanoparticles on graphene, which act as promising catalysts for one-step thermal decomposition of ammonium perchlorate at a fairly reduced temperature. Yitai group[47] have described hydrothermal process for the synthesis of branched mesoporous Mn_3O_4 nanorods by using potassium permanganate and poly(ethylene glycol) as starting materials. It was noted that the mesoporous nanorods are efficient catalysts for the degradation of methylene blue in the presence of H_2O_2 at 80 °C. It is, therefore, apparent that copious amount of reports on the synthesis and to study the catalytic activity of Mn_3O_4 particles are limited at the nanoscale. Moreover, during the past decade, much attention has been paid to investigations into the photocatalytic degradation of organic pollutants with metal oxide particles under UV light radiation.[48] Based on these perspectives, the synthesis of high surface area Mn_3O_4 superstructures and their application as photocatalysts could be investigated.

In this article, we have described the synthesis of dandelion-shaped Mn_3O_4 microstructures using dye/surfactant assemblies as soft-templates. The assemblies so formed have been characterised by absorption spectroscopy, FTIR, HRTEM, SEM, EDX, SAED, XRD and TGA analysis. The surface area of the particles has been measured by BET analysis. The catalytic activity of the particles has been screened by studying the photocatalytic degradation of an aqueous solution of alizarin red under visible light illumination.

2. Experimental section

2.1. Reagents and instruments

All the reagents used were of analytical reagent grade. Manganese(II) acetate tetrahydrate [$Mn(ac)_2 \cdot 4H_2O$], fluorescein isothiocyanate–dextran 2000S (FITC-D 2000S), cetyltrimethylammonium bromide (CTAB), alizarin red and diethanolamine (DEA) were purchased from Sigma Aldrich and were used without further purification. The dye, FITC-D 2000S is one of the major derivatives of fluorescein isothiocyanate and is available as a dark orange-yellow powder that is slightly soluble in water and alcohol. Cetyltrimethylammonium bromide is a cationic surfactant with critical micellar concentration of 0.92 mM at 25 °C. Double distilled water was used throughout the course of the investigation. A 0.1 mM aqueous (water : methanol = 95 : 5 v/v) solution of alizarin red was used as a stock solution. The temperature was 298 ± 1 K during the experiments.

Absorption spectra were measured in a Shimadzu UV-1601 digital spectrophotometer (Shimadzu, Japan) taking the sample in 1 cm well-stoppered quartz cuvette. High-resolution transmission electron microscopy was carried out on a JEOL JEM-2100 microscope with a magnification of 200 kV. Samples were prepared by placing a drop of solution on a carbon-coated copper grid and dried overnight under vacuum. Selected area electron diffraction pattern was obtained using the same microscope. Energy dispersive X-ray analysis was performed on an INCA Energy TEM 200 using an X-ray detector. Scanning electron micrographs were recorded by using JEOL JSM-6360 instrument equipped with a field emission cathode with a lateral resolution of approximately 3 nm and acceleration voltage 3 kV after sputtering the sample on silicon wafer with carbon (approx. 6 nm). Thin films were prepared by drop-coating from the methanolic solutions of the respective samples onto silicon wafers. Fourier transform infrared spectra were recorded in the form of pressed KBr pallets in the range (400–4000 cm^{-1}) with Shimadzu-FTIR

Prestige-21 spectrophotomèter. X-ray diffraction patterns were obtained using a D8 Advanced Broker AXS X-ray Diffractometer with CuK_α radiation ($\lambda = 1.4506$ Å); data were collected at a scan rate of 0.5° min^{-1} in the range of 10–80°. The powder specific surface area was measured by BET analysis using a Micromeritics Tristar 3000 surface area analyzer. Thermogravimetric analysis was carried out on a Perkin-Elmer STA 6000 with the sample under nitrogen with heating from 40–800 °C (rate: 10 °C min^{-1}) and then, maintained at 800 °C for half an hour. Before TGA measurements, the samples were dried overnight in vacuum oven at 50 °C. Photocatalytic reaction was carried out by a 60 watt tungsten lamp (Institute of Electric Light Source, Beijing) that was positioned inside a cylindrical Pyrex vessel and surrounded by a recirculating water jacket (Pyrex) to cool the lamp. A cut-off filter was placed outside the Pyrex jacket to completely remove wavelengths shorter than 420 nm and to ensure that irradiation was achieved by visible light wavelengths only.

2.2. Synthesis of Mn_3O_4 microdandelions using dye–surfactant composites

The superstructures of manganese oxide have been synthesised using dye–surfactant conjugates in a particular molar ratio and manganese acetate tetrahydrate as the precursor salt. In a typical synthesis, an aliquot of aqueous FITC-D 2000S (0.5 nM) was added to an aqueous solution of CTAB (10 μM) in double-necked round-bottom flask so that the total volume of the solution is 25 mL and the mixture was stirred overnight at room temperature. Now, an amount of 0.245 g $Mn(ac)_2 \cdot 4H_2O$ was dissolved in the dye–surfactant mixture by refluxing on a water bath at 65 °C. After complete dissolution of the precursor, 100 μL diethanolamine was added and refluxing was continued for another 6 h. After about 30 min, the reaction mixture, suddenly, turned into yellowish brown from a colourless solution indicating the formation of manganese oxide superstructures. As the refluxing was continued, the colour slowly changed into deep brown pointing out to the aggregation between the ultra-small manganese oxide particles. Then, the water bath was removed and the reaction mixture was stirred for 12 h at room temperature. The particles formed by this method was washed five times with slightly hot water and finally, dispersed in water. The manganese oxide nanoparticles prepared by this method are stable for a month and can be stored in the desiccator for several days without any significant agglomeration or precipitation of the particles.

2.3. Photocatalytic reaction

The photocatalytic activity of Mn_3O_4 microdandelions was tested by following the degradation of an organic dye, alizarin red in aqueous solution. The as-synthesised Mn_3O_4 microdandelions was annealed at 500 °C in argon atmosphere for 1 h to remove the organics so as to avoid any influence of the FITC-D 2000S or CTAB in the catalytic reaction. In the photocatalytic experiments, 25 μg of the dried catalysts was dispersed with 3.0 mL of 2.0 μM aqueous solution of the dye and the solution was stirred in the dark for 2 h to reach adsorption–desorption equilibrium between the catalysts and alizarin red. Then, the mixture was irradiated by a 60 W tungsten lamp and the progress of the reaction was followed in the absorption spectrophotometer.

3. Results and discussion

The as-synthesised superstructures so formed have been characterized by absorption spectroscopy, FTIR, HRTEM, SEM, EDX, SAED, XRD and TGA analysis. The absorption spectral features of the Mn_3O_4 particles in the solid state are shown in Fig. 1. The dye or the surfactant molecules do not exhibit any characteristic absorption spectral features in the prescribed low concentration (1.0 nM) employed for this experiment although FITC in aqueous medium shows a sharp absorption maximum at 289 nm and a broad absorption band with maximum at 490 nm at a certain higher concentration range.[49] The electronic absorption spectrum of assemblies shows three well-defined regions: the first portion from 220 to 300 nm, the second from 310 to 500 nm (with a maximum at 325 nm), and the third one finishing at 800 nm. The first portion is attributed to charge transfer transitions, and the last two can be, reasonably, related to d–d crystal field transitions, $^3E_g(G) \leftarrow {}^3T_{1g}$, $^3A_{2g}(F) \leftarrow {}^3T_{1g}$, $^3A_{2g}(G) \leftarrow {}^3T_{1g}$, $^3T_{2g}(H) \leftarrow {}^3T_{1g}$, $^3T_{1g}(H) \leftarrow {}^3T_{1g}$ and $^3E_g(H) \leftarrow {}^3T_{1g}$, on octahedral Mn^{3+} species corresponding to manganese oxide particles in the superstructures.[50] The appearance of a strong peak at around 325 nm is due to the allowed $O^{2-} \rightarrow Mn^{2+}$ and $O^{2-} \rightarrow Mn^{3+}$ charge transfer transitions.[51] These results indicate that manganese oxide particles are embedded in the dye or surfactant or dye–surfactant hybrid assemblies. The direct band gap energy (E_g) for the manganese oxide superstructures could be determined by fitting the absorption data to the direct band gap transition equation as,[52]

$$(\alpha h\nu)^2 = A(h\nu - E_g) \quad (1)$$

where, α is the absorption co-efficient, $h\nu$ the photon energy and A a constant. The absorption coefficient (α) is defined as: $\alpha = 2.303A/Lc$, where, A is the absorbance of the sample, c the loading of sample (g L^{-1}), L the path length (=1 cm). Profile showing a plot of $(\alpha h\nu)^2$ as a function of $h\nu$ is shown in panel b and the extrapolation of linear portions of the curve towards absorption equal to zero offers a measure of the direct band gap transitions, E_g. The estimated direct band gap of the Mn_3O_4 was found to be 1.302 eV; this value is considerably different from the reported value of bulk Mn_3O_4.[20] The conjugation of FITC-D 2000S/CTAB through effective intermolecular complexation between complementary binding sites on dye and surfactant molecules and the presence of manganese precursor led to synergistic effect in the formation of superstructures.[49]

The morphology, composition and crystallinity of the as-prepared Mn_3O_4 assemblies synthesised at the dye–surfactant conjugates are described in Fig. 2. Low resolution scanning electron micrograph (panel a) shows Mn_3O_4 nanobuilding units are self-assembled into micrometer-sized aggregates with dandelion-like appearances. Inset shows the photograph of a real dandelion showing the morphological resemblance with the particles. At a relatively higher resolution (panel b), flower-

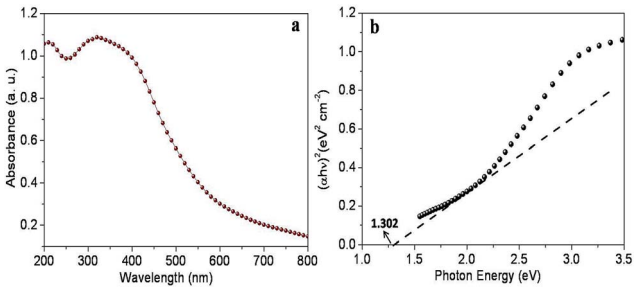

Fig. 1 (a) Solid state absorption spectrum and (b) plot of $(\alpha h\nu)^2$ as a function photon energy of Mn_3O_4 microdandelions in dye–surfactant conjugates.

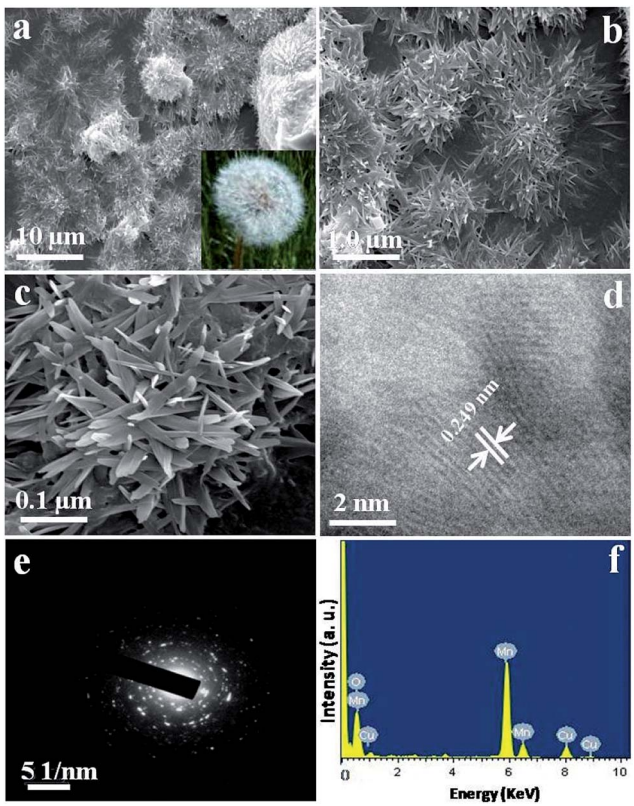

Fig. 2 (a–c) Scanning electron microscopic images of Mn_3O_4 microdandelions in dye–surfactant assemblies; (d) high resolution TEM, (e) selected area electron diffraction, and (f) electron diffraction X-ray spectrum. Inset in panel a shows the photograph of real dandelions to show the resemblance with the Mn_3O_4 microstructures.

like arrangements with average diameters *ca.* 1.0 μm is seen. At higher resolution (panel c), petals of the flowers are apparent that demonstrate adequate stabilisation of the nanoparticles with a high degree of organisational selectivity.[53] High resolution TEM image (panel d) of Mn_3O_4 microdandelions displays the interplanar distance between the fringes is about 0.249 nm which corresponds to the distance between the (211) planes of the Mn_3O_4 tetragonal crystal lattice. Selected area electron diffraction pattern (panel e) of the Mn_3O_4 particles is consistent with tetragonal Mn_3O_4 with strong ring patterns due to (101), (103) and (220) planes and therefore, confirms the crystallinity of the particles.[54] Representative energy dispersive X-ray spectrum (panel f) of Mn_3O_4 particles of dye–surfactant/manganese oxide hybrid assemblies reveals that the particles are composed of Mn, O, C elements. The signals of C, O and Cu elements come from the stabilizer dye, surfactant and the supporting TEM grid.

The formation of manganese oxide particles in the dye–surfactant conjugates have been seen through FTIR spectroscopy. Fig. 3 shows a comparison of the FTIR spectra for pure FITC-D 2000S/CTAB conjugates and the composite dye–surfactant/manganese oxide superstructures. In trace a, the FTIR spectrum of dye–surfactant conjugates shows the characteristic –N=C=S peak located at the region of 2333–2359 cm^{-1} along with the presence of aromatic –OH at 3163 cm^{-1} and the ether linkage at 1105 cm^{-1} corresponding to FITC-D 2000S, and C–N stretch at 1207 cm^{-1} corresponding to CTAB are seen.[49] It is observed that, in the conjugates, the intensities for nearly all of the vibrations are weakened and furthermore, several vibrations are missing, pointing out to the complexation between dye and surfactant molecules. In trace b, the band at 457 cm^{-1}, which is marked with a shadowed area, is the characteristic stretch of Mn–O indicating the formation of manganese oxide in the superstructures. The two absorption bands located at 2924 and 2852 cm^{-1} could be assigned to the symmetric and asymmetric stretching modes of the $-CH_2$ groups of the CTAB surfactant bound to the surface of Mn_3O_4, respectively.[55]

The X-ray diffraction pattern of the Mn_3O_4 microdandelions is shown in Fig. 4. Trace a is of the manganese oxide/dye–surfactant hybrid assemblies; all diffraction peaks implying a crystalline structure can be indexed to the tetragonal hausmannite structure with lattice parameters, $a = b = 5.762$ Å, and $c = 9.469$ Å and space group $I4_{1/amd}$, which are consistent with the standard values of bulk Mn_3O_4 (JCPDS# 24-0734). The Mn_3O_4 structures are, further, characterised by their chemical transformation under thermal toughening condition (trace b). After heating at 500 °C in argon atmosphere for 1 h, the peaks become sharpened and in addition, no additional diffraction peaks are seen suggesting excellent crystalline quality of the manganese oxide particles.[56]

Thermogravimetric analysis (Fig. 5) of the as-dried powder sample shows two weight loss steps in the curve: 3.5 wt% loss corresponding to the water desorption (up to 200 °C), and a weight loss of 17.5 wt% over 200–800 °C as a result of the decomposition of dye/surfactant assemblies, verifying that the dye/surfactant conjugates are, indeed, incorporated into the microstructures.[57] Since amphiphilicity is the molecular basis of the self-assembly for the dye–surfactant systems, it is imperative that by tuning the amphiphilicity of the building blocks, the process of self-assembly could be manipulated. To interpret the relative importance of the amphiphilicity of the dye molecules in designing dye–surfactant assembly, the interaction of FITC-dextran 2000S with the surfactant molecules has been elucidated. An unpredictably lower concentration of the CTAB solution is required to occur an indispensable interaction between the dye and surfactant molecules. As the formation of dye–surfactant aggregate is successful when the surfactant concentration is insufficient to form micelles and the sugar molecules

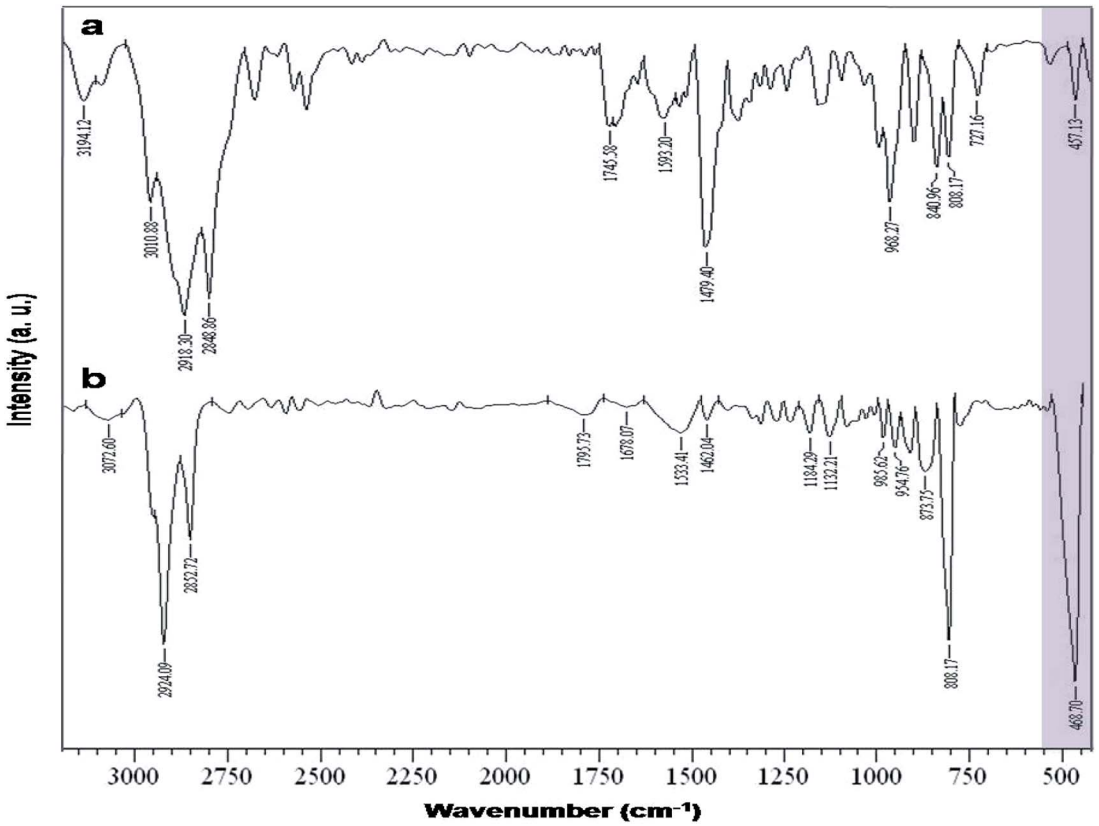

Fig. 3 FTIR spectra of (a) FITC-D 2000S/CTAB and (b) after formation of Mn_3O_4 microdendelions in FITC-D 2000S/CTAB soft template at room temperature.

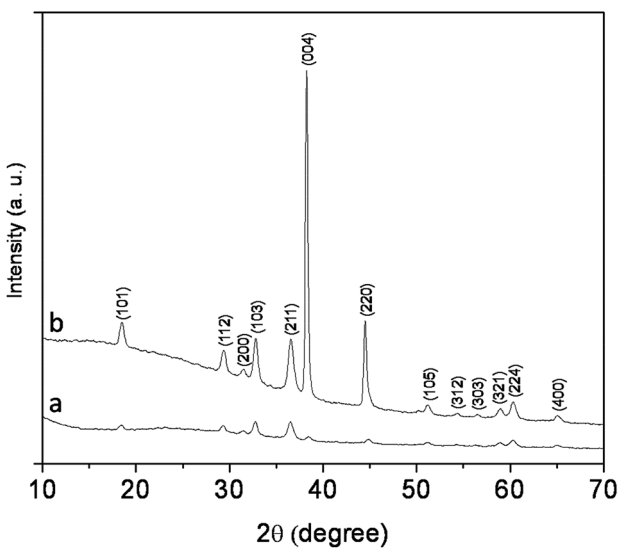

Fig. 4 X-ray diffraction patterns of manganese oxide/dye–surfactant hybrid assemblies (a) as-prepared and (b) after calcinations at 500 °C for 1 h in argon atmosphere.

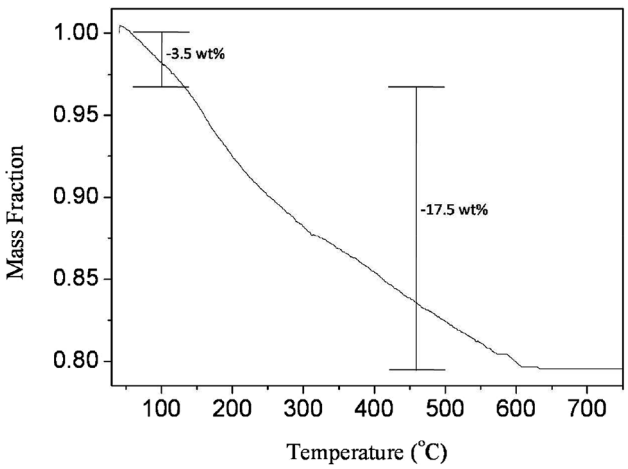

Fig. 5 Thermogravimetric analysis of the Mn_3O_4 microdandelions/dye–surfactant hybrid assemblies as-dried in air.

are not surface-active, authenticates the importance of amphiphilicity of the dye molecules in manufacturing hybrid assembly to act as soft-template for preparation of manganese oxide superstructures.[49] A plausible mechanism of the formation of Mn_3O_4 microdandelions using dye–surfactant composites could be enunciated as follows. Addition of manganese acetate precursor to the dye–surfactant mixture results in the binding of Mn(II) to the dye–surfactant conjugates[58] and subsequent hydrolysis governs the formation of Mn_3O_4 microstructures with dandelions-like morphology.[59] A schematic presentation of the evolution of Mn_3O_4 microdandelions using dye–surfactant composites is shown in Scheme 1.

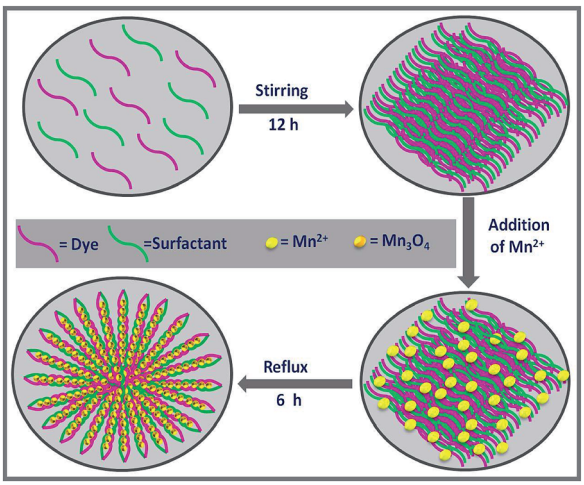

Scheme 1 Schematic presentation showing the formation of Mn_3O_4 microdandelions at the dye–surfactant assemblies.

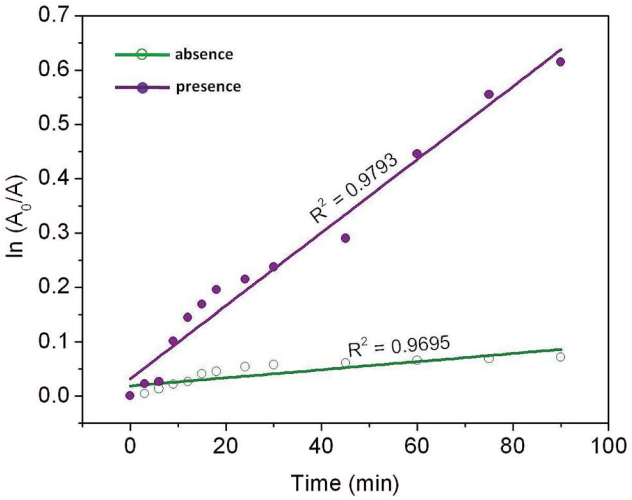

Fig. 7 Plot of $\ln(A_0/A)$ as a function of time for the degradation of alizarin red in the absence and presence of Mn_3O_4 microdandelions under visible light irradiation.

The textural properties of the as-dried powder sample of Mn_3O_4 microdandelions have been characterised by Brunauer–Emmett–Teller (BET)[60] gas-sorption measurements performed at 77 K under vacuum. The specific surface area and Langmuir surface area of the microstructures have been measured to be *ca.* 15.76 and 25.81 $m^2\ g^{-1}$, respectively which are higher than that of the commercial Mn_3O_4 ($0.9 \pm 1.8\ m^2\ g^{-1}$).[61] Therefore, it is evident that Mn_3O_4 microdandelions, synthesised in the present experiment, manifest higher BET surface area to provide a platform for the photocatalytic degradation of organic dye molecules.[62] A comparative account of the surface area in the bulk and nano dimension of the Mn_3O_4 microdandelions and some other manganese oxides-based catalysts[53,61,63] is shown in ESI 1.†

To assess the photocatalytic activity of these Mn_3O_4 microstructures, the degradation of alizarin red was selected as the model reaction. Alizarin red or 1,2-dihydroxyanthraquinone, also known as 'Turkey Red', is an organic dye belonging to alizarin family, derived from the roots of plants of the madder genus and has been used as a prominent red dye, especially, for dyeing textile fabrics.[64] The photocatalytic degradation of alizarin red was employed as the model reaction as its degradation can, easily and quantitatively, be monitored *via* its absorption spectroscopy. Moreover, alizarin red was chosen because of its high stability against spontaneous photobleaching in the absence of a photocatalyst.[65] In the photocatalytic reaction, 25 μg of the as-prepared catalysts was dispersed with 3.0 mL of 2.0 μM aqueous solution of the dye molecules and the progress of the reaction was followed in the absorption spectrophotometer. Fig. 6 shows the absorption spectral changes during the photocatalytic degradation of alizarin red in aqueous medium. The

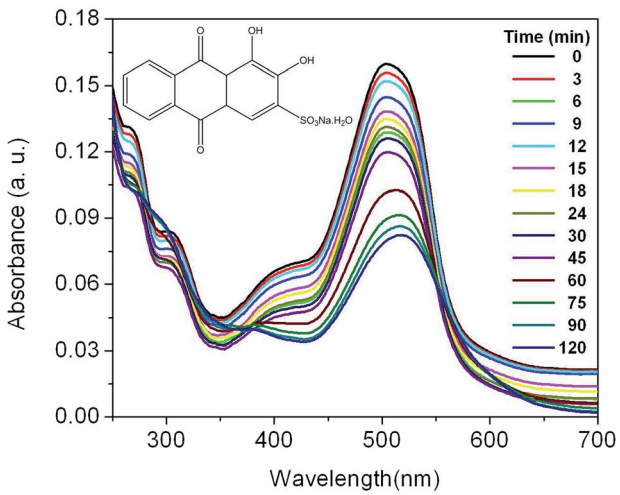

Fig. 6 Absorption spectral changes of aqueous solution of alizarin red (2.0 μM) in the presence of 25 μg Mn_3O_4 under visible light irradiation. Inset shows the molecular structure of the dye.

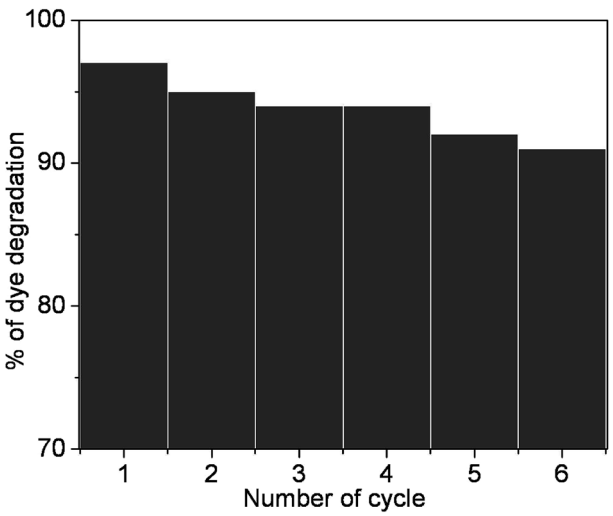

Fig. 8 Histogram showing the percentage of the degradation of the dye in each cycle.

Table 1 A comparative account of the catalytic activity of the visible light photocatalysts for alizarin red degradation

Catalysts	Particle size (nm)	Reaction conditions	Catalyst loading ($g\ L^{-1}$)	Reaction rate (min^{-1})	Reference
TiO_2 nanostructures	8 ± 2	500 W halogen lamp	0.5	0.084	Liu *et al.*[30]
Bi-doped TiO_2	30 ± 10	150 W Philips bulb, wavelength 420–520 nm	0.025	0.0232	Sood *et al.*[31]
CdS nanostructures	—	pH ~ 8.4	0.05	0.0169	Patil *et al.*[34]
TiO_2–In_2O_3 nanocomposites	8–12	Pen Ray lamp of 4400 μW cm^{-2}	0.1	0.0058	Rodríguez-González *et al.*[35]
TiO_2	10–12	Photolysis, ultrasonication	0.03	0.0225	Vinu *et al.*[39]
Mn_3O_4 microdandelions	1000 ± 200	60 W tungsten bulb, room temp.	0.008	0.0067	Present work

molecular structure of the dye is shown in the inset. The dye molecules exhibit a very intense absorbance band centered around 503 nm along with a less intense vibrational shoulder, centered around 308 nm corresponding to $n \rightarrow \pi^*$ and $\pi \rightarrow \pi^*$ transitions and molar extinction coefficient, $\varepsilon \sim 29\,100\ M^{-1}\ cm^{-1}$ corresponding to the monomeric form of the dye.[66] As controls, an aqueous solution of alizarin red (3.0 mL, 2.0 μM) was exposed to the same tungsten lamp under identical experimental conditions. It was observed that, in the absence of the catalysts, the degradation of the dye is very slow in the experimental time scale. To check whether absorbance decrease is a result of alizarin red absorption, we have mixed the dye and Mn_3O_4 microdandelions at the experimental concentrations and allowed to equilibrate overnight under vacuum. Only a slight decrease in the absorbance of the dye was seen; thus, the possibility of the absorbance decrease as a result of alizarin red absorption could be ruled out. As control experiment, the influence of only FITC-D 2000S or CTAB at the concentrations that may be present in the microdandelions employed for the photocatalytic reaction has been tested. It was noted that pure dye or surfactant does not bear any influence on the photocatalytic degradation of the dye molecules. The degradation of the dye, also, does not take place in the absence of light. Therefore, it could be conceived that Mn_3O_4 microstructures are indispensable for the visible light-assisted degradation of the dye molecules.

In the presence of Mn_3O_4 microdandelions, alizarin red molecules start to degrade upon visible light illumination. With increase in irradiation time, the intensity of alizarin red ($\lambda_{max} \sim$ 505 nm) decreases sharply. After a certain time ($t = 30$ min), the intensity at 505 nm decreases and the intensity at 270 and 295 nm increases. These changes in the absorption spectral features indicate that with increase in irradiation time alizarin red undergoes photocatalytic degradation and forms small fragmented organic products.[31,36] Under visible light irradiation, dyes rather than Mn_3O_4 particles are excited by visible light to appropriate singlet and triplet states, subsequently, followed by electron injection from the excited dye onto the conduction band of metal oxides, whereas the dyes are converted to the cationic dye radicals, $dye^{\bullet+}$.[31] The injected electron of Mn_3O_4 (e^-) reacts with pre-adsorbed O_2 to form oxidising species ($O_2^{\bullet-}$, $HOO^\bullet$ and then $^\bullet OH$ radicals) that can bring about photooxidations. The major component of the peroxides produced is H_2O_2, CO_2 and to smaller carbonyl species; the principal intermediate produced is phthalic acid.[31] Thus, metal oxide nanoparticles play an important role in electron transfer mediation, even, though itself is not excited.

Profile showing the plot $\ln(A_0/A)$ where, A_0 is the absorbance at $t = 0$ and A the absorbance at time $t = t$, as a function of time is presented in Fig. 7. It is, apparent, that the reaction follows first-order kinetics and corresponding rate constants were calculated to be 1.9×10^{-4} and $6.7 \times 10^{-3}\ min^{-1}$ in the absence and presence of the catalysts, respectively which indicate that the rate of reaction is enhanced by approximately 35 times in the presence of the Mn_3O_4 microdandelions.

In this reaction, Mn_3O_4 microdandelions act as heterogeneous catalysts which are inorganic materials.[67,68] It is observed that the catalysts could be reused up to six cycles of operations without any apparent loss of activity. Therefore, the catalysts were separated from the reaction mixture by centrifugation or natural sedimentation at the end of the degradation reaction and subsequent drying in air. A histogram showing the percentage of the degradation of the dye in each cycle is presented in Fig. 8. A comparative account of the nano/microstructured catalysts for the photocatalytic degradation of alizarin red under visible light irradiation has been presented in Table 1. Therefore, it could be conceived that Mn_3O_4 microdandelions could be employed as alternative catalysts for the degradation of alizarin red under visible light irradiation.

4. Conclusions

In conclusion, the cumulative effect of the FITC-dextran 2000S/CTAB assemblies have been exploited for synthesis of high surface area Mn_3O_4 microdandelions. The microstructures were found to act as effective catalysts for the degradation of alizarin red under visible light illumination. The dye–surfactant conjugates could be exploited as soft-templated system for the synthesis of other inorganic materials with controlled morphological superstructures and unusual functionalities.

Acknowledgements

We gratefully acknowledge financial support from DBT, New Delhi (Project No. BT/277/NE/TBP/2013).

References

1 N. A. Kotov, In *Nanoparticle Assemblies and Superstructures*, CRC Press, Boca Raton, USA, 2005.
2 M. Grzelczak, J. Vermant, E. M. Furst and L. M. Liz-Marzán, *ACS Nano*, 2010, **4**, 3591–3605.
3 H. Cölfen and M. Antonietti, *Angew. Chem., Int. Ed.*, 2005, **44**, 5576–5591.
4 W. T. S. Huck In *Nanoscale Assembly: Chemical Techniques*, Springer, India, 2005.
5 K. J. Bishop, C. E. Wilmer, S. Soh and B. A. Grzybowski, *Small*, 2009, **5**, 1600–1630.
6 D. M. Vriezema, M. C. Aragones, J. A. A. W. Elemans, J. J. L. M. Cornelissen, A. E. Rowan and R. J. M. Nolte, *Chem. Rev.*, 2005, **105**, 1445–1489.
7 H. Chen, J. He, C. Zhang and H. He, *J. Phys. Chem. C*, 2007, **111**, 18033–18038.
8 A. K. Sinha, M. Pradhan and T. Pal, *J. Phys. Chem. C*, 2013, **117**, 23976–23986.
9 Z. Chen, Z. Jiao, D. Pan, Z. Li, M. Wu, C.-H. Shek, C. M. L. Wu and J. K. L. Lai, *Chem. Rev.*, 2012, **112**, 3833–3855.
10 S. K. Bikkarolla, F. Yu, W. Zhou, P. Joseph, P. Cumpson and P. Papakonstantinou, *J. Mater. Chem. A*, 2014, **2**, 14493–14501.
11 L. Que Jr and W. B. Tolman, *Nature*, 2008, **455**, 333–340.
12 R. J. K. Taylor, M. Reid, J. Foot and S. A. Raw, *Acc. Chem. Res.*, 2005, **38**, 851–869.
13 S. L. Brock, N. Duan, Z. R. Tian, O. Giraldo, H. Zhou and S. L. Suib, *Chem. Mater.*, 1998, **10**, 2619–2628.
14 M. Amini, M. M. Najafpour, S. Nayeri, B. Pashaei and M. Bagherzadeh, *RSC Adv.*, 2012, **2**, 3654–3657.
15 S. K. Ghosh, J. Kang, M. Inokuchi and N. Toshima, *Appl. Catal., A*, 2013, **464**, 225–232.
16 I. Djerdj, D. Arčon, Z. Jagličić and M. Niederberger, *J. Phys. Chem. C*, 2007, **111**, 3614–3623.
17 P. Li, C. Nan, Z. Wei, J. Lu, Q. Peng and Y. Li, *Chem. Mater.*, 2010, **22**, 4232–4236.
18 N. Birkner, S. Nayeri, B. Pashaei, M. M. Najafpour, W. H. Casey and A. Navrotsky, *Proc. Natl. Acad. Sci. U. S. A.*, 2013, **110**, 8801–8806.
19 A. Ramírez, P. Hillebrand, D. Stellmach, M. M. May, P. Bogdanoff and S. Fiechter, *J. Phys. Chem. C*, 2014, **118**, 14073–14081.
20 S. Yin, X. Wang, Z. Mou, Y. Wu, H. Huang, M. Zhu, Y. Du and P. Yang, *Phys. Chem. Chem. Phys.*, 2014, **16**, 11289–11296.
21 S. Liu, Z. R. Tang, Y. Sun, J. C. Colmenares and Y. Xu, *Chem. Soc. Rev.*, 2015, **44**, 5053–5075.
22 N. Zhang, M.-Q. Yang, S. Liu, Y. Sun and Y.-J. Xu, *Chem. Rev.*, 2015, **115**, 10307–10377.
23 M.-Q. Yang, N. Zhang, M. Pagliaro and Y.-J. Xu, *Chem. Soc. Rev.*, 2014, **43**, 8240–8254.
24 P. V. Kamat, *J. Phys. Chem. Lett.*, 2012, **3**, 663–672.
25 S. K. Dutta, S. K. Mehetor and N. Pradhan, *J. Phys. Chem. Lett.*, 2015, **6**, 936–944.
26 A. Fujishima and K. Honda, *Nature*, 1972, **238**, 37–40.
27 P. Zucca, C. Vinci, F. Sollai, A. Rescigno and E. Sanjust, *J. Mol. Catal. A: Chem.*, 2008, **288**, 97–102.
28 M. Panizza and M. A. Oturan, *Electrochim. Acta*, 2011, **56**, 7084–7087.
29 L. Qifu, N. Guohua, J. Yiman, W. Wenwei and M. Yuedong, *Plasma Sci. Technol.*, 2014, **16**, 1036–1041.
30 G. Liu, X. Li, J. Zhao, S. Horikoshi and H. Hidaka, *J. Mol. Catal.*, 2000, **153**, 221–229.
31 S. Sood, S. K. Mehta, A. Umar and S. K. Kansal, *New J. Chem.*, 2014, **38**, 3127–3136.
32 S. K. Kansal, R. Lamba, S. K. Mehta and A. Umar, *Mater. Lett.*, 2013, **106**, 385–389.
33 S. Siva Kumar, V. Ranga Rao and G. Nageswara Rao, *Proc. Natl. Acad. Sci., India, Sect. A*, 2013, **83**, 309–315.
34 B. N. Patil, D. B. Naik and V. S. Shrivastava, *Adv. Sci. Lett.*, 2011, **4**, 11–12.
35 V. Rodríguez-González, F. Paraguay-Delgado, X. García-Montelongo, L. M. Torres–Martínez and R. Gómez, *J. Ceram. Proc. Res.*, 2008, **9**, 606–610.
36 H. Lachheb, E. Puzenat, A. Houas, M. Ksibi, E. Elaloui, C. Guillard and J.-M. Herrmann, *Appl. Catal., B*, 2002, **39**, 75–90.
37 P. Tian, L. Sun, G. Liu, Y. H. Kang, J. D. Duan and W. L. Du, *Adv. Mater. Res.*, 2013, **643**, 170–173.
38 V. J. Babu, R. S. R. Bhayatharini and S. Ramakrishna, *RSC Adv.*, 2014, **4**, 19251–19256.
39 R. Vinu and G. Madras, *Environ. Sci. Technol.*, 2009, **43**, 473–479.
40 J. Wu, J. Cao, W.-Q. Han, A. Janotti and H.-C. Kim, In Functional Metal Oxide Nanostructures, *Springer Series in Materials Science*, Springer, New York, 2012.
41 Y. Yang, L. Zhu, X. Yang, E. Shao, X. Deng, N. Liu and M. Wu, *J. Mater. Chem. A*, 2015, **3**, 2934–2941.
42 P. Zhang, Y. Zhan, C. C. Hao, J. Wang, C. Liu, Z. Meng, Z. Yin and W. Chen, *Nano Res.*, 2010, **3**, 235–243.
43 R. Tarik, P. Jean-Yves, S. Lorette, H. Frédéric, B. Emmanuel, B. Marc and A. Ahmed, *Appl. Catal., A*, 2010, **386**, 132–139.
44 H. Nishita, H. Hashimoto, N. Kimura, N. Miyata, T. Fuji, B. Ohtani and J. Takada, *RSC Adv.*, 2012, **2**, 6420–6423.
45 A. Khalid, A. Mohamed, Z. Qiumei, W. Kangbing and K. Huang, *J. Solid State Chem.*, 2010, **183**, 744–751.
46 N. Li, G. Zhenfeng, C. Minhua, R. Ling, Z. Xinyu, L. Bing, T. Yuan and C. Hu, *Carbon*, 2013, **54**, 124–132.
47 B. Zhongchao, S. Bo, F. Na, J. Zhicheng, L. Menghua, X. Liqiang and Q. Yitai, *Chem.–Eur. J.*, 2012, **18**, 5319–5324.
48 M. A. Fox and M. T. Dulay, *Chem. Rev.*, 1993, **93**, 341–357.
49 S. K. Ghosh, M. Ali and H. Chatterjee, *Chem. Phys. Lett.*, 2013, **561–562**, 147–152.
50 W. S. Kijlstra, E. K. Poels, A. Bliek, B. M. Weckhuysen and R. A. Schoonheydt, *J. Phys. Chem. B*, 1997, **101**, 309–316.
51 A. Vázquez-Olmos, R. Redón, A. L. Fernández-Osorio and J. M. Saniger, *Appl. Phys. A*, 2005, **81**, 1131–1134.
52 S. Tsunekawa, T. Fukuda and A. Kasuya, *J. Appl. Phys.*, 2000, **87**, 1318–1321.
53 H. Rahaman, R. M. Laha, D. K. Maiti and S. K. Ghosh, *RSC Adv.*, 2015, **5**, 33923–33929.
54 A. Giri, N. Goswami, M. Pal, M. Tay, Z. Myint, S. Al-Harthi, A. Singha, B. Ghosh, J. Dutta and S. K. Pal, *J. Mater. Chem. C*, 2013, **1**, 1885–1895.

55 T. Ahmad, K. V. Ramanujachary, S. E. Lofland and A. K. Ganguli, *J. Mater. Chem.*, 2004, **14**, 3406–3410.
56 J. W. Lee, A. S. Hall, J.-D. Kim and T. E. Mallouk, *Chem. Mater.*, 2012, **24**, 1158–1164.
57 H.-P. Cong and S.-H. Yu, *Adv. Funct. Mater.*, 2007, **17**, 1814–1820.
58 A. Mehra and P. Venkateswarlu, *J. Chem. Phys.*, 1968, **48**, 4381–4383.
59 S. Xie, X. Zhou, X. Han, Q. Kuang, M. Jin, Y. Jiang, Z. Xie and L. Zheng, *J. Phys. Chem. C*, 2009, **113**, 19107–19111.
60 S. Brunauer, P. H. Emmett and E. Teller, *J. Am. Chem. Soc.*, 1938, **60**, 309–319.
61 S. K. Sahu, B. Huang, K. Lilova, B. F. Woodfield and A. Navrotsky, *Phys. Chem. Chem. Phys.*, 2015, **17**, 22286–22295.
62 N. Birkner and A. Navrotsky, *Proc. Natl. Acad. Sci. U. S. A.*, 2014, **111**, 6209–6214.
63 D. Su, H.-J. Ahn and G. Wang, *J. Mater. Chem. A*, 2013, **1**, 4845–4850.
64 A. Claro, M. J. Melo, S. Schäfer, J. S. S. de Melo, F. Pina, K. J. van den Berg and E. Aviva Burnstock, *Talanta*, 2008, **74**, 922–929.
65 G. Liu, T. Wu, J. Zhao, H. Hidaka and N. Serpone, *Environ. Sci. Technol.*, 1999, **33**, 2081–2087.
66 C. Miliani, A. Romani and G. Favaro, *J. Phys. Org. Chem.*, 2000, **13**, 141–150.
67 F. Polzer, S. Wunder, Y. Lu and M. Ballauff, *J. Catal.*, 2012, **289**, 80–87.
68 K. Laurier, F. Vermoortele, R. Ameloot, D. E. de Vos, J. Hofkens and M. Roeffaers, *J. Am. Chem. Soc.*, 2013, **135**, 14488–14491.

RSC Advances

PAPER

Cite this: *RSC Adv.*, 2015, **5**, 33923

Fabrication of Mn_2O_3 nanorods: an efficient catalyst for selective transformation of alcohols to aldehydes†

Hasimur Rahaman,[a] Radha M. Laha,[b] Dilip K. Maiti*[b] and Sujit Kumar Ghosh*[a]

Received 9th February 2015
Accepted 24th March 2015

DOI: 10.1039/c5ra02504d

www.rsc.org/advances

A facile wet chemical approach has been devised for the preparation of self-assembled, high surface area, nanostructured Mn_2O_3 through an effective polymer–surfactant interaction. Its outstanding catalytic property for the selective transformation of alcohols to aldehydes has been reported. The polyethylene glycol/sodium dodecyl sulphate conjugates act as soft templates for the formation of manganese oxide nanorods upon treatment of a weak base, namely, diethanolamine, with manganese acetate as a precursor under mild refluxing conditions. The Mn_2O_3 nanorods were found to be efficient and selective catalysts for the synthesis of valuable aldehydes and ketones over undesirable acid by-products using a low catalyst loading. The precursor alcohols bearing activated and unactivated aromatic rings, double and triple bonds, and chiral sugar moiety were tolerated in this direct oxidative transformation strategy developed under benign reaction conditions.

1. Introduction

Catalysts are the work-horses in synthetic chemistry.[1–3] The robust reactivity and selectivity of catalysts lead to the efficient transformation of raw materials into the desired pharmaceuticals, fuels, agrochemicals, pigments, polymers, commercial and natural compounds, which are essential for our highly demanding modern society. In this context, nanomaterials have tremendous potential to serve as catalysts with significantly improved performance because of their active surface and interfacial atom effect, innovative new chemical property, high reactivity, low catalyst loading, environmentally benign nature, easy recovery and reusability.[4–20] In recent years, the size and shape-controlled synthesis of manganese oxides (MnO_x) nanomaterials has attracted considerable interest from both academia and industry due to their tuneable physicochemical properties and applications in[9–12] high-density magnetic storage media,[13] ion-exchange,[14] molecular adsorption,[15] electronics,[16] biosensors,[17] energy storage,[18] batteries[19] and catalysts.[20] Manganese oxides are the most attractive inorganic materials owing to their structural flexibility and availability of different oxidation states of manganese (II, III and IV), which are responsible for their structural, transport and magnetic properties[21–24] in a diverse range of niche applications.[25–27] Among the different oxidation states of manganese oxides, Mn_2O_3 is well-known as a cheap and environmentally friendly catalyst and could be employed as an ideal candidate for the removal of CO and NO_x from waste gas,[28] decomposition of H_2O_2 into hydroxyl radicals in the catalytic peroxidation of organic effluents[29] and as an oxygen storage component.[30] Although catalytic activities over transition metal oxide catalysts are lower than those over noble metal catalysts, the inherent advantages of metal oxide catalysts, such as low cost, high thermal stability, and high mechanical strength, make them a promising alternative for outstanding catalytic applications.[31] The catalytic activity of these materials at the nanoscale dimension depends strongly on their surface properties, while the reactivity and selectivity of nanoparticles can be tuned through controlling the morphology because the exposed surfaces of the particles have distinct crystallographic planes depending on their shape.[32] Therefore, the synthesis of Mn_2O_3 nanoparticles with well-controlled morphology and a narrow size distribution is desirable for achieving practical applications such as catalysis.

Diverse synthetic approaches have been implemented in the literature for the fabrication of size and shape-selective Mn_2O_3 nanostructures, and their physical and chemical properties have been exploited in a wide range of applications. Ganguli and co-authors prepared nanorods of anhydrous manganese oxalate as a precursor to synthesize single phase nanoparticles of various manganese oxides, such as MnO, Mn_2O_3 and Mn_3O_4, under specific reaction conditions and studied their field-dependent magnetization properties.[33] Han and co-workers reported the synthesis of Mn_2O_3 nanocrystals by the

[a]*Department of Chemistry, Assam University, Silchar-788011, India. E-mail: sujit.kumar.ghosh@aus.ac.in; Fax: +91-3842-270802; Tel: +91-3842-270848*

[b]*Department of Chemistry, University of Calcutta, Kolkata-700009, India. E-mail: dkmchem@caluniv.ac.in*

† Electronic supplementary information (ESI) available: Characterization details of synthesized materials, reaction schemes, catalysis details with tables. See DOI: 10.1039/c5ra02504d

thermolysis of manganese(III) acetyl acetonate on a mesoporous silica, SBA-15, and the nanocomposites showed significant catalytic activity toward CO oxidation below 523 K.[34] Chen and He described a facile synthesis of mono-dispersed Mn_2O_3 nanostructures by treating a mixture of $KMnO_4$ solution and oleic acid at low temperatures (below 200 °C) and have demonstrated the application of these particles as efficient water purifiers.[35] Polshettiwar *et al.* devised a simple strategy using an aqueous solution of $K_3[Mn(CN)_6]$ under microwave irradiation to afford a nanomaterial.[12] Gnanam and Rajendran described the preparation of α-Mn_2O_3 nanoparticles by dropwise addition of an aqueous ammonia solution to manganese(II) chloride tetrahydrate ($MnCl_2 \cdot 4H_2O$) in methanol with vigorous stirring and reported the optical properties of the synthesized materials.[36] Yang *et al.* reported the size-controlled synthesis of monodispersed Mn_2O_3 octahedra assembled from nanoparticles by a mediated *N*,*N*-dimethylformamide solvothermal route, and the particles were found to exhibit catalytic activity towards CO oxidation.[37] Qiu *et al.* described the synthesis of hierarchically structured Mn_2O_3 nanomaterials with different morphologies and pore structures from precursors containing the target materials interlaced with the polyol-based organic molecules and examined their potential as anode materials for lithium ion batteries.[38] Cao *et al.* reported large-scale synthesis of Mn_2O_3 homogeneous core/hollow-shell structures with cube-shaped and dumbbell-shaped morphologies, and the particles were found to exhibit an excellent performance in waste water treatment.[39] Najafpour *et al.* described the synthesis of nano-sized Mn_2O_3 particles by the decomposition of an aqueous solution of manganese nitrate at 100 °C, and it was observed that the particles possessed catalytic activities towards the water oxidation and epoxidation of olefins in the presence of cerium(IV) ammonium nitrate and hydrogen peroxide, respectively.[40] We envisioned the fabrication of Mn_2O_3 nanorods by a soft-template strategy, which will provide a roughened high surface area to offer an ideal platform for high and innovative chemical activity towards novel catalysis processes such as the most demanding direct synthesis of aldehydes and ketones from alcohols under oxidative conditions.

Aldehydes are valuable compounds and one of the most frequently used ingredients of organic synthesis in industry and academia. The tremendous importance of this class of compounds is supported by the development of enormous methodologies for their synthesis reported in the literature.[41–45] The direct oxidative transformation of alcohols to aldehydes is a fundamental organic reaction. This approach suffers from a serious drawback of the generation of a large quantity of the corresponding acid[43] as a by-product because the transformation of acid from the *in situ* generated desired aldehyde is more energetically favourable than the oxidation of alcohol to aldehyde. Thus, with the advent of synthesising metallic nanomaterials, silver, gold, palladium, ruthenium and platinum nanoparticles are utilized under basic and/or stringent reaction conditions for the oxidation of alcohol to aldehyde.[44,45] To improve the substrate scope, selectivity and versatility in the catalytic dehydrogenation process, we envisioned using calcined manganese oxide nanorods and λ^3-hypervalent iodane[46,47] as a stoichiometric oxidant under neutral and benign reaction conditions (Scheme 1). In this article, we have reported an innovative approach to fabricate rod-shaped Mn_2O_3 nanostructures using a polymer–surfactant assembly as a soft-template, and their catalytic activity is discovered towards the selective oxidation of alcohols to valuable aldehydes, chiral analogues and ketones using phenyliododiacetate [$PhI(OAc)_2$] as an oxidizing agent.

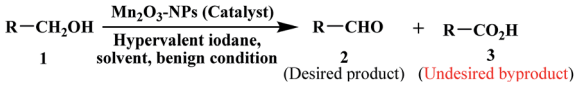

Scheme 1 Direct synthesis of aldehydes using Mn_2O_3-nanorods catalyst.

2. Experimental

2.1 Reagents and instruments

All the reagents used were of analytical reagent grade. Manganese(II) acetate tetrahydrate, diethanolamine (DEA), polyethylene glycol (PEG-400), sodium dodecyl sulphate (SDS) and phenyliodoacetate ($PhI(OAc)_2$) were purchased from Sigma Aldrich and were used without further purification. Double distilled water was used throughout the course of the investigation. The temperature was maintained at 298 ± 1 K during the experiments.

Absorption spectra were measured using a Shimadzu UV-1601 digital spectrophotometer (Shimadzu, Japan) by placing the sample in a 1 cm well-stoppered quartz cuvette. The surface and structural morphologies of Mn_2O_3 samples were studied by scanning electron microscopic (SEM) images, which were recorded using a JSM-6360 (JEOL) instrument equipped with a field emission cathode having a lateral resolution of approximately 3 nm by applying an acceleration voltage of 3 kV after sputtering the sample on a silicon wafer with carbon (approx. 6 nm). Thin films were prepared by drop-coating the aqueous-methanolic solutions of the respective samples onto silicon wafers. Transmission electron microscopy was carried out on a JEOL JEM-2100 microscope operating at 200 kV. Samples were prepared by placing a drop of solution on a carbon-coated copper grid and drying overnight under vacuum. High-resolution transmission electron micrographs and selected area electron diffraction (SAED) pattern were obtained using the same JEOL JEM-2010 instrument, operating at 200 kV. Energy dispersive X-ray (EDX) analysis was performed on an INCA Energy TEM 200 using an X-ray detector. Fourier transform infrared (FTIR) spectra were recorded in the form of pressed KBr pellets in the range of 400–4000 cm^{-1} with a Shimadzu-FTIR Prestige-21 spectrophotometer. The powder X-ray diffraction patterns were obtained using a D8 Advanced Bruker axs X-ray Diffractometer with CuK_α radiation ($\lambda = 1.540589$ Å); data were collected at a scan rate of 0.5° min^{-1} in the range of 10–80°. Raman scattering measurements were carried out on a silicon substrate in the backscattering geometry using a fiber-coupled micro-Raman spectrometer equipped

with a 488 nm (2.55 eV), 5 mW air-cooled Ar^+ laser as the excitation light source, a spectrometer (model TRIAX550, JY) and a CCD detector. The powder specific surface area was measured by BET analysis using a Micromeritics Tristar 3000 surface area analyzer. Thermogravimetric analysis was carried out on a Perkin-Elmer STA 6000 with a sample amount of 10 mg. The measurements were performed under nitrogen with heating from 40–800 °C (rate: 10 °C min^{-1}), and then maintaining at 800 °C for half an hour. Before TGA measurements, the samples were dried overnight in a vacuum oven at 50 °C.

2.2 Synthesis of manganese oxide nanorods in polymer–surfactant conjugates

The nanostructures of manganese oxide were synthesised using polymer–surfactant conjugates and manganese acetate tetrahydrate as the precursor salt. In a typical synthesis, an aliquot of aqueous polyethylene glycol (PEG) (0.4 mmol dm^{-3}) was added to an aqueous solution of sodium dodecyl sulphate (SDS) (2 mmol dm^{-3}) in a two-necked round-bottom flask such that the total volume of the solution was 25 mL, and the mixture was stirred overnight at room temperature. Then, 0.245 g of $Mn(ac)_2 \cdot 4H_2O$ was dissolved in the polymer–surfactant mixture by refluxing on a water bath at 65 °C. After the complete dissolution of the precursor, 100 μL diethanolamine was added and refluxing was continued for another 6 h. After about 30 min, the reaction mixture turned yellowish brown from a colourless solution indicating the formation of manganese oxide nanostructures. As the refluxing was continued, the colour slowly changed to deep brown, indicating the aggregation of the ultrasmall manganese oxide particles to rod shaped nanostructures. The water-bath was removed and the reaction mixture was stirred for 12 h at room temperature. The particles formed by this method were washed five times with slightly hot water and finally dispersed in water. The manganese oxide nanostructures prepared by this method are stable for a month and can be stored in a vacuum desiccator without any significant agglomeration or precipitation of the particles.

2.3 General procedure for the synthesis of aldehydes

The precursor alcohol (1 mmol), Mn_2O_3 (1.6 mg, 0.01 mmol), $PhI(OAc)_2$ (403 mg, 1.25 mmol) and $MgSO_4$ (about 300 mg) were placed together in ethylenedichloride (EDC, 25 mL) and stirred magnetically at 45 °C until the reaction was complete. The progress of the reaction was monitored by TLC. After the completion of the reaction, the post reaction mixture was filtered through a sintered funnel and the residue was washed with EDC (2 × 5 mL). The combined EDC was transferred to a separating funnel, washed with water (3 × 10 mL) and dried using activated $MgSO_4$. The solvent was removed using a rotary evaporator at room temperature under reduced pressure. The crude product was purified by column chromatography over silica gel (60–120 mesh) using ethyl acetate–petroleum ether as eluent to afford the desired aldehyde and corresponding acid byproduct. Thus, the reaction of benzyl alcohol (**1a**, 109 mg, 1.0 mmol) afforded benzaldehyde (**2a**) and benzoic acid (**3a**) after purification by column chromatography on silica gel (60–120 mesh) with ethyl acetate–petroleum ether (1 : 200, v/v) as an eluent in yields of 87% (92.5 mg, 0.87 mmol) and 4% (4.5 mg, 0.04), respectively. The structures of the desired product (**2a**) and by-product (**3a**) were confirmed with the help of the boiling and melting points available in the literature; moreover, the recorded NMR (^1H and ^{13}C), FT-IR, and mass (HR-MS) spectra were compared with those available in the literature. Similarly, other aldehydes (**2b–e**), ketones (**4a** and **b**), acids (**3a–f**) and sugar aldehyde (**2f**) were characterized by measuring melting/boiling points and recording NMR (^1H and ^{13}C), FT-IR, and mass (HR-MS) spectra and optical rotation, which were verified with the data and spectra reported in the literature.

3. Results and discussion

In the present study, we have reported an innovative fabrication approach for rod-shaped Mn_2O_3 nanostructures using a polymer–surfactant assembly as a soft-template, and their catalytic activity towards the selective oxidation of alcohols to valuable aldehydes, chiral analogue and ketones using phenyliododiacetate [$PhI(OAc)_2$] as an oxidizing agent has been investigated.

The absorption spectral features of the as-synthesized Mn_2O_3 sample in the solid state are shown in ESI 1.† The estimated direct band gap of the Mn_2O_3 was found to be 1.29 eV; this value is almost close to the reported value of Mn_2O_3 nanostructures.[48] The morphology, composition and crystallinity of the particles synthesized using the polymer–surfactant mixture are presented in Fig. 1. The representative scanning electron micrograph (trace a) of the Mn_2O_3 particles shows a bunch of elongated nanorods with length up to 1 ± 0.3 μm and width of 50 ± 10 nm. To further examine the surface morphology of the microstructures, high magnification SEM images were recorded (trace b), and it was apparent that the surface of the particles had roughened edges, which indicates that the growth and slow transformation to rod-shaped nanostructures occur through the oriented aggregation of primary nanocrystals. At the very beginning of reflux, the concentration of reactants is comparatively high; therefore, some nuclei can be formed rapidly, resulting in the occurrence of ultrasmall particles. Subsequently, the nuclei orient and grow fast along the (211) direction to form one-dimensional nanorods.[49] The size and shape of the nanocrystals is further evident from the transmission electron micrographs (panel c) of the Mn_2O_3 particles formed using the polymer–surfactant assembly. The high resolution TEM image (panel d) of the Mn_2O_3 nanorods displays an interplanar distance of about 0.357 nm between the fringes, which corresponds to the distance between the (211) planes of the Mn_2O_3 crystal lattice.[50] The selected area electron diffraction pattern (panel e) of the Mn_2O_3 nanostructures is consistent with strong ring patterns due to (211), (222) and (400) planes, which confirms the crystallinity of the materials.[51] The representative energy dispersive X-ray spectrum (panel f) of Mn_2O_3 nanorods indicates that the particles are composed of Mn and O elements. The formation of manganese oxide particles in the polymer–surfactant conjugates has been studied

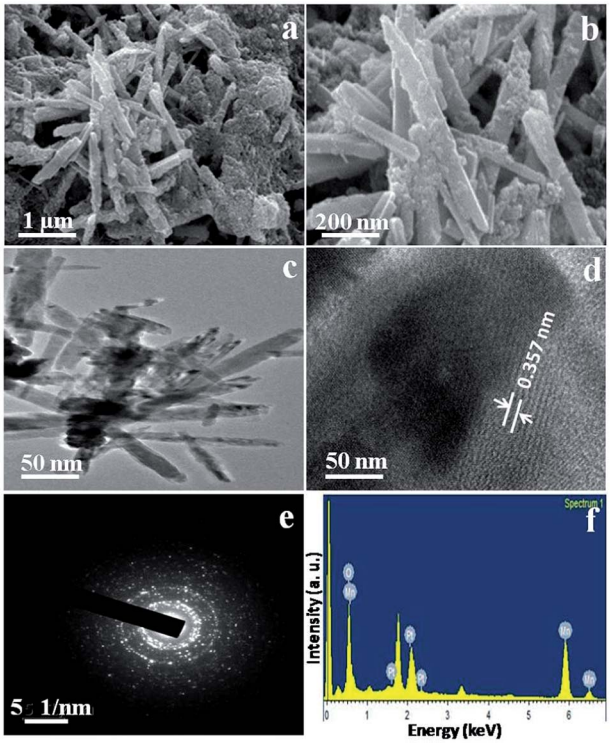

Fig. 1 (a) Scanning electron micrograph, (b) high resolution scanning electron micrograph, (c) transmission electron micrograph, (d) high resolution transmission electron micrograph, (e) selected area electron diffraction pattern, and (e) energy dispersive X-ray analysis of the manganese oxide microrods in polymer–surfactant conjugates.

through FTIR spectroscopy (ESI 2†). It is seen that an Mn–O bond stretching frequency appears in the range of 450–680 cm^{-1} along with two strong peaks at 630 and 525 cm^{-1}, which arise due to the stretching vibration of Mn–O and Mn–O–Mn bonds,[35] indicating the formation of Mn_2O_3 in the polymer–surfactant conjugates.[52] The X-ray diffraction pattern of the representative hybrid rod-shaped assemblies is shown in ESI 3;† all diffraction peaks, implying a crystalline structure, are consistent with the standard values of bulk Mn_2O_3 [JCPDS no. 41-1442].[34] Fig. 2 shows the Raman spectrum of the as-prepared nanorods under ambient condition. The structure of Mn_2O_3 belongs to Ia_3 symmetry group with $a = 9.41$ and possesses cubic bixbyite structures.[53] The bands at 310, 366 and 655 cm^{-1} could be ascribed to the out-of-plane bending modes of Mn_2O_3, the asymmetric stretch of bridge oxygen species (Mn–O–Mn) and the symmetric stretch of Mn_2O_3, respectively,[54,55] in correspondence to that obtained for bulk MnO*x* particles.[56]

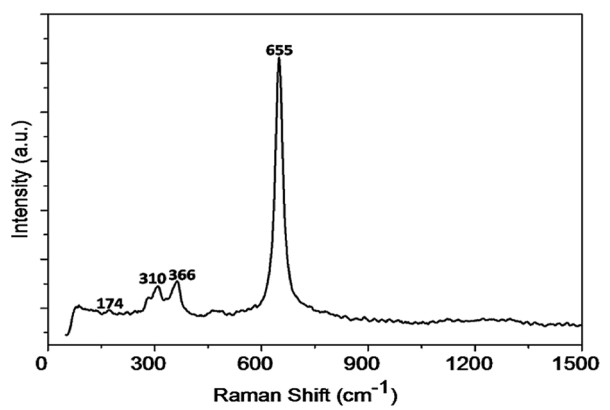

Fig. 2 Raman spectrum of the manganese oxide/polymer–surfactant hybrid assemblies dried in air.

Thermogravimetric analysis (ESI 4†) of the as-dried powder sample shows two weight loss steps in the curve: 8.9 wt% loss corresponding to the water desorption (up to 200 °C) and a weight loss of 32.1 wt% over 200–800 °C as a result of the decomposition of polymer–surfactant assemblies, verifying that the polymer–surfactant conjugates are, indeed, incorporated into the nanostructures.[57] The textural properties of the Mn_2O_3 microrods were investigated by Brunauer–Emmett–Teller (BET) gas-sorption measurements performed at 77 K for the as-dried powder sample under vacuum, as shown in ESI 5.† The specific surface area and Langmuir surface area of the microrods were measured to be *ca.* 13.60 $m^2\ g^{-1}$ and 22.27 $m^2\ g^{-1}$, respectively, from which it is evident that Mn_2O_3 nanorods synthesised in the present experiment manifest high BET surface areas to provide a platform for the catalytic organic transformation.[30,58]

In the initial experiments, we decided not to apply a high temperature for the desired catalytic oxidation (Scheme 1) of our model substrate, benzylalcohol (**1a**, R = Ph, shown in ESI 6†) to benzaldehyde (**2a**) using λ^3-hypervalent iodane;[46,47,59] thus, the possibility of forming byproduct benzoic acid (**3a**, entry 1, Table 1) could be avoided. After several experiments using as-synthesised Mn_2O_3 nanorods (1 mol%), we discovered its catalytic property for the oxidative dehydrogenation reaction using PhIO[46] (1.25 mmol), which revealed about 60% conversion at 50 °C to afford benzaldehyde (**2a**; yield: 45%) with high selectivity (**2a** : **3a** = 9 : 1). The yield (68%) was improved when $PhICl_2$ (entry 2) was used. Gratifyingly, utilizing commercially available $PhI(OAc)_2$,[47] the conversion (100%), reaction rate (2 h), yield (96%) and selectivity (**2a** : **3a** = 47 : 3) were significantly improved under the similar reaction conditions (entry 3). The optimized oxidation process was found to utilize as low as 0.01 mol% of the nanorods as described in the entry 7, which was obtained (entries 5–8) by changing the reaction temperature (50–40 °C) and catalyst loading (1–0.005). The reaction rate (70% in 12 h), yield (48%) and selectivity (**2a** : **3a** = 2 : 3) were drastically reduced in the absence of the Mn_2O_3-NPs (entry 9). Ethylene dichloride was found to be the suitable solvent because the other polar aprotic solvents such as dichloromethane (CH_2Cl_2), tetrahydrofuran (THF) and acetonitrile (entries 10–12), nonpolar toluene (entry 13) and protic methanol or water (entries 14 and 15) were not effective for the unprecedented catalytic process.

The diverse catalytic activity of the Mn_2O_3-nanorods was evaluated utilizing various types of alcohols under the optimized reaction conditions (entry 1, Table 2 as shown in ESI 6†). The benzyl alcohols bearing activated (**1b**) and deactivated (**1c**) aromatic moieties (entries 2 and 3, Table 2†) were tolerated in this reaction to afford the corresponding aldehyde with

Table 1 Synthesized aldehydes, sugar aldehyde and ketones

Entry	Alcohol (1)	Catalyst	Reagent & conditions	Conversion (%)	Desired aldehyde (2) or ketone (4)	Acid (3)	Yield (%, 2 : 3)
1	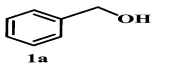 1a	Mn_2O_3 (0.01 mol%)	$PhI(OAc)_2$, EDC, 45 °C 4.0 h	100	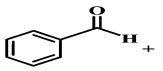 2a:96%	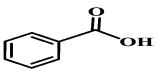 3a:4%	91 (24 : 1)
2	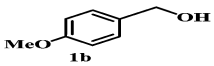 1b	Mn_2O_3 (0.01 mol%)	$PhI(OAc)_2$, EDC, 45 °C 4.5 h	100	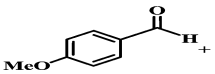 2b:95%	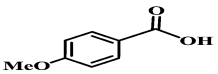 3b:5%	89 (19 : 1)
3	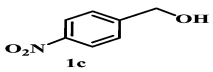 1c	Mn_2O_3 (0.01 mol%)	$PhI(OAc)_2$, EDC, 45 °C 3.0 h	100	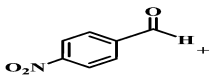 2c: 92%	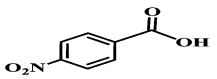 3c: 8%	95 (23 : 2)
4	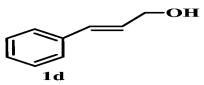 1d	Mn_2O_3 (0.01 mol %)	$PhI(OAc)_2$, EDC, 45 °C 4.0 h	100	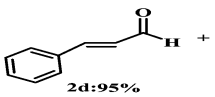 2d:95%	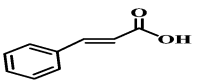 3d:5%	90 (19 : 1)
5	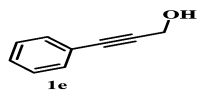 1e	Mn_2O_3 (0.01 mol %)	$PhI(OAc)_2$, EDC, 45 °C 4.0 h	100	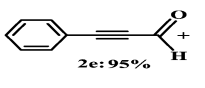 2e: 95%	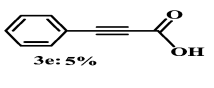 3e: 5%	92 (19 : 1)
6	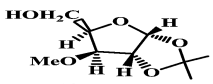 1f	Mn_2O_3 (0.01 mol%)	$PhI(OAc)_2$, EDC, 45 °C 4.0 h	100	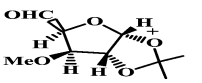 2f: 91%	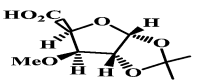 3f: 9%	76 (91 : 9)
7	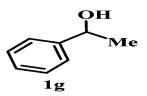 1g	Mn_2O_3 (0.02 mol%)	$PhI(OAc)_2$, EDC, 45 °C 6.0 h	100	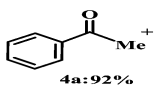 4a:92%	3a (not detected)	
8	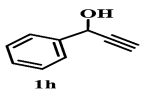 1h	Mn_2O_3 (0.02 mol%)	$PhI(OAc)_2$, EDC, 45 °C 5.0 h	100	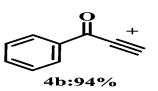 4b:94%	3a (not detected)	

excellent yield and selectivity (entries 2 and 3). Interestingly, in the presence of the strongly electron withdrawing $-NO_2$ group, the reaction rate was enhanced (from 4.5 to 3 h) with respect to the activated aromatic nucleus (**1b**), which simultaneously reduced the selectivity from 19 : 1 to 23 : 2 (entries 2 and 3).

The diverse catalytic activity of the Mn_2O_3-nanorods was evaluated utilizing various types of alcohols under the optimized reaction conditions (entry 1, Table 2†). The benzyl alcohols bearing activated (**1b**) and deactivated (**1c**) aromatic moieties (entries 2 and 3, Table 2†) were tolerated in this reaction to afford corresponding aldehyde with excellent yield and selectivity (entries 2 and 3). Interestingly, in the presence of strongly electron withdrawing $-NO_2$ group, the reaction rate was enhanced (from 4.5 to 3 h) with respect to the activated aromatic nucleus (**1b**), which simultaneously reduced the selectivity from 19 : 1 to 23 : 2 (entries 2 and 3). Another interesting feature observed in this reaction is the high chemoselectivity. Even the oxidation prone double and triple bond-bearing allyl (**1d**) and propargyl (**1e**) alcohols (entries 4 and 5) smoothly underwent oxidation to corresponding aldehydes with 90–92% yield and outstanding selectivity (19 : 1). We turned our attention to applying this benign strategy for the oxidation of sugar-based chiral alcohol (**1f**, entry 6), and under the similar reaction conditions it afforded corresponding optically pure aliphatic aldehyde (**2f**) with high yield (76%) and selectivity (91 : 9). The diverse catalytic activity of the Mn_2O_3-nanorods was also successfully exploited on functionalized secondary alcohols (**1g** and **1h**) to obtain corresponding ketones (**4a** and **4b**, entries 8 and 9) without the formation of the by-product, benzoic acid (**3a**). The catalytic reaction was tested with bulk Mn_2O_3, and it was seen that the particles could not selectively transform the alcohols to aldehydes. A comparative account highlighting the utility of Mn_2O_3 nanorods and some other catalysts[60–63] towards the oxidation of alcohols is presented in ESI 7.† This unprecedented property of Mn_2O_3-nanorods under very low catalyst loading (0.01 mol%) provides new prospects and perspectives in catalysis towards the discovery of new materials, innovative catalytic activity and novel organic transformation to afford functional molecules for our highly demanding modern society.

4. Conclusion

In conclusion, the hydrolysis of manganese precursor in the presence of polymer–surfactant soft template has been found to be an effective strategy for the fabrication of Mn_2O_3 nanorods. The nanorods are crystalline and offer roughened surface and large surface area that installs new and innovative catalytic

activity such as the direct synthesis of valuable aldehydes through the oxidation of alcohols in a highly chemoselective fashion. This new synthetic strategy for low dimensional manganese oxide materials could be exploited for the fabrication of novel inorganic materials with controlled superstructures and unusual functionalities. This unprecedented catalytic activity of Mn_2O_3 nanorods provides new prospects and perspectives in catalysis for the pursuance of novel organic transformations to afford functional molecules for our highly demanding modern society.

Acknowledgements

We gratefully acknowledge financial support from DBT, New Delhi (project no. BT/277/NE/TBP/2013) and DST, Nanomission, Govt. of India (project no. SR/NM/NS-29/2010). We are also thankful to CRNN, University of Calcutta for providing microscope facility to analyse the Mn_2O_3-microrods.

References

1 G. Rothenberg, *Catalysis*, Wiley, VHC, Weinheim, 2008.
2 M. Peplow, *Nature*, 2013, **495**, S10–S11.
3 S. Ghosh, S. Khamarui, K. S. Gayen and D. K. Maiti, *Sci. Rep.*, 2013, **3**, 2987.
4 M. Turner, V. B. Golovko, O. P. H. Vaughan, P. Abdulkin, A. Berenguer-Murcia, M. S. Tikhov, B. F. G. Johnson and R. M. Lambert, *Nature*, 2008, **454**, 981–984.
5 K. S. Gayen, T. Sengupta, Y. Saima, A. Das, D. K. Maiti and A. Mitra, *Green Chem.*, 2012, **14**, 1589–1592.
6 V. Polshettiwar, J.-M. Basset and D. Astruc, *ChemSusChem*, 2012, **5**, 6–8.
7 B. C. Ranu, D. Saha, D. Kundu and N. Mukherjee, in *Nanocatalysis: Synthesis and Applications of Aryl Carbon-Heteroatom Coupling Reactions using Nano-Metal Catalyst* ed. V. Polshettiwar and T. Asefa, Wiley-VCH, 2013.
8 R. S. Varma, *Sustainable Chem. Processes*, 2014, **2**, 11.
9 Z. Chen, Z. Jiao, D. Pan, Z. Li, M. Wu, C.-H. Shek, C. M. L. Wu and K. L. L. Joseph, *Chem. Rev.*, 2012, **112**, 3833–3855.
10 W. Weifeng, C. Xinwei, C. Weixing and G. I. Douglas, *Chem. Soc. Rev.*, 2011, **40**, 1697–1721.
11 G. S. Thomas, J. R. Bargar, S. Garrison and M. T. Bradley, *Acc. Chem. Res.*, 2010, **43**, 2–9.
12 V. Polshettiwar, B. Baruwati and R. S. Varma, *ACS Nano*, 2009, **3**, 728–736.
13 Z. Hao, C. Gaoping, W. Zhiyong, Y. Yusheng, S. Zujin and G. Zhennan, *Nano Lett.*, 2008, **8**, 2664–2668.
14 Y. Hirao, C. Yokoyama and M. Makoto, *Chem. Commun.*, 1996, 597–598.
15 E. A. Kotomin, Y. A. Mastrikov, E. Heifets and J. Maier, *Phys. Chem. Chem. Phys.*, 2008, **10**, 4644–4649.
16 Z. W. Chen, S. Y. Zhang, S. Tan, J. Wang and S. Z. Jin, *Appl. Phys. A*, 2004, **78**, 581–584.
17 S. Huang, Y. Ding, Y. Liu, L. Su, R. Filosa Jr and Y. Lei, *Electroanalysis*, 2001, **23**, 1912–1920.
18 J.-H. Kim, K. H. Lee, L. J. Overzet and G. S. Lee, *Nano Lett.*, 2011, **11**, 2611–2617.
19 M. M. Thackeray, C. S. Johnson, J. T. Vaughey, N. Li and S. A. Hackney, *J. Mater. Chem.*, 2005, **15**, 2257–2267.
20 O. Giraldo, S. L. Brock, W. S. Willis, M. Marquez and S. L. Suib, *J. Am. Chem. Soc.*, 2000, **122**, 9330–9331.
21 S. K. Nayak and P. Jena, *Phys. Rev. Lett.*, 1998, **81**, 2970–2973.
22 E. Lidstrom and O. Hartmann, *J. Phys.: Condens. Matter*, 2000, **12**, 4969–4974.
23 J. E. Pask, D. J. Singh, I. I. Mazin, C. S. Hellberg and J. Kortus, *Phys. Rev. B: Condens. Matter Mater. Phys.*, 2001, **64**, 024403.
24 I. Djerdj, D. Arčon, Z. Jagličić and M. Niederberger, *J. Phys. Chem. C*, 2007, **111**, 3614–3623.
25 R. Ma, Y. Bando, L. Zhang and T. Sasaki, *Adv. Mater.*, 2004, **16**, 918–922.
26 F. Y. Cheng, J. A. Shen, B. Peng, Y. D. Pan, Z. L. Tao and J. Chen, *Nat. Chem.*, 2011, **3**, 79–84.
27 Y. Oaki and H. Imai, *Angew. Chem., Int. Ed.*, 2007, **119**, 5039–5043.
28 H. M. Zang and Y. Teraoka, *Catal. Today*, 1989, **6**, 155–162.
29 B. Ammundsen and J. Paulsen, *Adv. Mater.*, 2001, **13**, 943–956.
30 Y. F. Chang and J. C. McCarty, *Catal. Today*, 1996, **30**, 163–170.
31 P. Serp, K. Philippot, G. A. Somorjai and B. Chaudret, *Nanomaterials in Catalysis*, Wiley-VCH, Winheim, Germany, 2013.
32 L. Hu, Q. Peng and Y. Li, *J. Am. Chem. Soc.*, 2008, **130**, 16136–16137.
33 A. Tokeer, K. V. Ramanujachary, S. E. Lofland and G. Ashok, *J. Mater. Chem.*, 2004, **14**, 3406–3410.
34 Y.-F. Han, F. Chen, Z. Zhong, K. Ramesh, L. Chen and E. Widjaja, *J. Phys. Chem. B*, 2006, **110**, 24450–24456.
35 C. Hongmin and H. Junhui, *J. Phys. Chem. C*, 2008, **112**, 17540–17545.
36 S. Gnanam and V. Rajendran, *J. Sol-Gel Sci. Technol.*, 2011, **58**, 62–69.
37 L. Liu, H. Liang, H. Yang, J. Wei and Y. Yanzhao, *Nanotechnology*, 2011, **22**, 015603–015611.
38 Y. Qiu, G.-L. Xu, K. Yan, H. Sun, J. Xiao, S. Yang, S.-G. Sun, L. Jin and H. Deng, *J. Mater. Chem.*, 2011, **21**, 6346–6353.
39 J. Cao, Q. Mao and Y. Qian, *J. Solid State Chem.*, 2012, **191**, 10–14.
40 M. Amini, M. M. Najafpour, S. Nayeri, B. Pashaei and M. Bagherzadeh, *Dalton Trans.*, 2012, **41**, 11026–11031.
41 T. Mallat and A. Baiker, *Chem. Rev.*, 2004, **104**, 3037–3058.
42 C. J. Weiss, P. Das, D. L. Miller, M. L. Helm and A. M. Appel, *ACS Catal.*, 2014, **4**, 2951–2958.
43 D. Könning, T. Olbrisch, F. D. Sypaseuth, C. C. Tzschucke and M. Christmann, *Chem. Commun.*, 2014, **50**, 5014–5016.
44 Y. Hong, X. Yan, X. Liao, R. Li, S. Xu, L. Xiao and J. Fan, *Chem. Commun.*, 2014, **50**, 9679–9682.
45 Z.-A. Qiao, P. Zhang, S.-H. Chai, M. Chi, G. M. Veith, N. C. Gallego, M. Kidder and S. Dai, *J. Am. Chem. Soc.*, 2014, **136**, 11260–11263.
46 D. K. Maiti, N. Chatterjee, P. Pandit and S. K. Hota, *Chem. Commun.*, 2010, **46**, 2022–2024.
47 S. Khamarui, R. Maiti and D. K. Maiti, *Chem. Commun.*, 2015, **51**, 384–387.

48 Q. Javed, F.-P. Wang, M. Y. Rafique, A. M. Toufiq and M. Z. Iqbal, *Chin. Phys. B*, 2012, **21**(1–7), 117311.
49 Y. Li, H. Tan, O. Lebedev, J. Verbeeck, E. Biermans, G. van Tendeloo and B.-L. Su, *Cryst. Growth Des.*, 2010, **10**, 2969–2976.
50 G. Yang, W. Yan, J. Wang and H. Yang, *CrystEngComm*, 2014, **16**, 6907–6913.
51 L. Ling, L. Hui, Y. Hongxiao, W. Jingjing and Y. Yanzhao, *Nanotechnology*, 2011, **22**, 015603–015611.
52 S. K. Ghosh, M. Ali and H. Chatterjee, *Chem. Phys. Lett.*, 2013, **561**, 147–152.
53 C. M. Julien, M. Massot and C. Poinsignon, *Spectrochim. Acta, Part A*, 2004, **60**, 689–700.
54 Y. T. Chua, P. C. Stair and I. E. Wachs, *J. Phys. Chem. B*, 2001, **105**, 8600–8606.
55 F. Buciuman, F. Patcas, R. Cracium and D. R. T. Zahn, *Phys. Chem. Chem. Phys.*, 1999, **1**, 185–190.
56 Y. Luo, Y.-Q. Deng, W. Mao, X.-J. Yang, K. Zhu, J. Xu and Y.-F. Han, *J. Phys. Chem. C*, 2012, **116**, 20975–20981.
57 H.-P. Cong and S.-H. Yu, *Adv. Funct. Mater.*, 2007, **17**, 1814–1820.
58 S. Brunauer, P. H. Emmett and E. Teller, *J. Am. Chem. Soc.*, 1938, **60**, 309–319.
59 M. Uyanik and K. Ishihara, *Chem. Commun.*, 2009, 2086–2099.
60 J. Zhu, K. Kailasam, A. Fischer and A. Thomas, *ACS Catal.*, 2011, **1**, 342–347.
61 H. Caot and S. L. Suib, *J. Am. Chem. Soc.*, 1994, **116**, 5334–5342.
62 X. Fu, J. Feng, H. Wang and K. M. Ng, *Nanotechnology*, 2009, **20**, 375601–375610.
63 J. Chen, J. C. Lin, V. Purohit, M. B. Cutlip and S. L. Suib, *Catal. Today*, 1997, **33**, 205–214.

RSC Advances

COMMUNICATION

View Article Online
View Journal | View Issue

Cite this: *RSC Adv.*, 2014, **4**, 41976

Received 2nd June 2014
Accepted 21st August 2014

DOI: 10.1039/c4ra05240d

www.rsc.org/advances

Bifunctional gold–manganese oxide nanocomposites: benign electrocatalysts toward water oxidation and oxygen reduction†

Hasimur Rahaman, Koushik Barman, Sk Jasimuddin and Sujit Kumar Ghosh*

Gold–manganese oxide nanocomposites were synthesised by seed-mediated epitaxial growth at the water/*n*-heptane interface under mild reflux conditions. These nanocomposites exhibit efficient electrocatalytic activity toward the water oxidation reaction (WOR) and the simultaneous oxygen reduction reaction (ORR) at a low overpotential ($\eta \approx 370$ mV) and under neutral pH conditions.

1. Introduction

Industrial scale production of clean energy could replace finite fossil fuels with abundant, renewable, environmentally benign energy sources and would lead to the survival of the planet in a sustainable manner that poses a significant challenge to humanity in the 21st century.[1,2] There is a growing need for electrocatalytic water oxidation to produce dioxygen for the conversion of electrical energy to stored chemical energy in the form of fuels.[3,4] Plants utilize complex catalytic systems for the breakdown of water into its elements. In nature and in many protocols designed for artificial photosynthesis, water oxidation, $2H_2O \rightarrow 4H^+ + O_2 + 4e^-$, is a key step and hence our better understanding of these systems could pioneer new designs of effective catalysts.[5,6] The activity of electrocatalysts for water oxidation is of fundamental importance for the development of promising energy conversion technologies, including integrated solar water-splitting devices, water electrolyzers, and lithium–air batteries.[7] Therefore, to meet future challenges, water oxidation has become an important area of research, which is inspired by energy challenges and bioinspired by the emerging understanding of photosystem II.[8,9] The salient features of the technical impediments to such a reaction is the requirement of efficient and inexpensive electrocatalysts capable of oxidizing water to drive this energetically highly unfavorable reaction ($\Delta H^\circ = 572$ kJ mol^{-1}).[10] Several protocols have been adopted in the literature to design efficient, inexpensive and robust electrocatalysts for the water oxidation reaction based on metallic platinum,[11] various oxides and complexes of iridium,[12] ruthenium,[13] nickel,[14] cobalt,[15] iron[16] and copper complexes,[17] and to evaluate the oxygen evolution activity in acidic and/or alkaline conditions Amongst the materials considered so far for water oxidation catalysts, first row transition metal oxides can are abundant and have reasonable stability compared with their noble metal analogues.[18]

In particular, manganese oxides are materials of considerable importance due to their interesting structural, magnetic and transport properties that arise from their excellent structural flexibility combined with novel chemical and physical properties.[19] Among the series of manganese oxides available in various oxidation states of manganese (II, III, IV), Mn_3O_4 (hausmannite) has been found to be an effective and inexpensive catalyst in a number of oxidation and reduction reactions.[20] On the other hand, gold nanoparticles have also attracted increasing attention due to their unique properties, such as high biocompatibility, tunable electronic and optical behavior, good conductivity and high catalytic activity, which make them fundamental building blocks for the development of innovative functional materials.[21] The assembly of different nanomaterials with specific optical, magnetic, or electronic properties to multicomponent composites can change and even enhance the properties of the individual constituents.[22] Bifunctional composite nanostructures containing gold have found tremendous importance in the field of nanocatalysis due to the rich surface chemistry of gold.[23] The fabrication of nanocomposites containing two or more different functionalities has also started attracting attention due to their enhanced catalytic properties.[24]

Several reports have been published in the literature using manganese oxides and complexes as electrocatalysts for water oxidation. Dismukes *et al.*[25] described the thermodynamic and

Department of Chemistry, Assam University, Silchar 788011, India. E-mail: sujit.kumar.ghosh@aus.ac.in; Fax: +91-3842-270802; Tel: +91-3842-270848

† Electronic supplementary information (ESI) available: Experimental details, cyclic voltammogram, digital camera images and reaction schemes. See DOI: 10.1039/c4ra05240d

mechanistic aspects that Nature appears to use for catalyzing *in vitro* water oxidation by photosynthesis using bioinspired and photoactive Mn_4O_4-cubane clusters. Drawing inspiration from the cubane-like CaMn(4)O(x), the biological catalyst found in the oxygen evolving centre in the photosystem II, Gorlin and Jaramillo[26] investigated the electrocatalytic activity of nanostructured manganese oxide surfaces that exhibited similar oxygen electrode activity to the best known precious metal nanoparticle catalysts, *viz.*, platinum, ruthenium and iridium. In a recent communication, Jaramillo and colleagues[27] demonstrated the addition of Au to MnO_x to produce an order of magnitude higher turnover frequency than that of the best pure MnO_x catalysts and a local, rather than bulk, interaction between Au and MnO_x, which led to the observed enhancement in the activity of the reaction. Zaharieva and co-authors[28] showed that the binuclear manganese molecular complex $[(OH_2)(terpy)Mn(\mu\text{-}O)_2Mn(terpy)(OH_2)]^{3+}$, which is the most prominent structural and functional model of the water-oxidizing manganese complexes operating in plants and cyanobacteria, could be supported on montmorillonite clay and, using Ce(IV) as a chemical oxidant, the complex could act as one of the best manganese-based molecular catalyst toward water oxidation. Wiechen *et al.*[29] reported the syntheses of layered manganese oxides, where the interlayer cations, *viz.*, K-, Ca-, Sr- and Mg-containing birnessites, were varied and also observed that the oxygen-evolving complex required the presence of calcium in their structures to achieve maximum catalytic activity. Spiccia and co-workers[30] showed that for the nanoparticulates of manganese oxides, formed in Nafion polymer, the catalytic activity toward the water oxidation was dependent on the dispersivity of the nanoparticles. They also reported synthetic methodologies for the preparation of highly active mixed valent MnO_x catalysts by the partial oxidation of crystalline $Mn^{II}O$ nanoparticles and analysed the catalytic activity in water splitting devices.[31] In a review, the group elucidated the perspectives of a cluster that contains four manganese and one calcium ions bridged by five oxygen atoms in a distorted chair-like arrangement in the current structural and mechanistic understanding of the oxygen evolving complex in photosystem II.[32] Being inspired by the structural diversity of manganese oxides that occur naturally as minerals in at least 30 different crystal structures, Dismukes and colleagues[33] chose to systematically compare eight synthetic oxide structures containing Mn(III) and Mn(IV) with cubic phases, and concluded that electronically degenerate Mn(III) imparts lattice distortions, due to the Jahn–Teller effect, that are hypothesized to contribute to the structural flexibility, which is important for catalytic turnover in water oxidation at the surface. Suib and group[34] compared the catalytic activity of mixed valent porous amorphous manganese oxides, cryptomelane-type tunnel manganese oxides, and layered birnessite as water oxidation catalysts, and observed that amorphous manganese oxides exhibit significantly higher turnovers compared to tunnel and layered structures. In spite of all these investigations with molecular and solid-state electrocatalysts capable of mediating water oxidation, many fundamental questions and practical challenges remain, and clear improvements are needed in cost, durability, and overpotential.

In this communication, we have explored the controllable integration into gold–manganese oxide nanocomposites by seed-mediated epitaxial growth at the water/*n*-heptane interface, and also investigated the electrocatalytic activity of the combinatorial catalysts toward water oxidation and oxygen reduction at low overpotential (370 mV) and, most importantly, under neutral pH conditions.

2. Experimental section

2.1. Reagents and instruments

All the reagents used were of analytical reagent grade. Gold(III) chloride trihydrate ($HAuCl_4 \cdot 3H_2O$, ≥99.9%), trisodium citrate (≥99%), manganese acetate tetrahydrate ($Mn(ac)_2 \cdot 4H_2O$), 4-aminothiophenol (4-ATP), and phosphoric acid were obtained from Sigma Aldrich and were used as received. Sodium perchlorate, sodium hydroxide, methanol, *n*-heptane, and ammonia were purchased from Sisco Research Laboratories, India, and were used without further purification. An aliquot of 0.1 M phosphate buffer saline (PBS) was prepared by mixing an equimolar solution of phosphoric acid and sodium perchlorate, followed by the dropwise addition of sodium hydroxide. Double-distilled water was used throughout the course of the investigations. The temperature was 298 ± 1 K for all experiments.

Absorption spectra were recorded in a Shimadzu UV-1601 digital spectrophotometer (Shimadzu, Japan), taking the sample in a 1 cm well-stoppered quartz cuvette. Transmission electron microscopy (TEM) was carried out on a JEOL JEM-2100 microscope with a magnification of 200 kV. Samples were prepared by placing a drop of solution onto a carbon coated copper grid and drying overnight under vacuum. Dark field scanning tunneling electron micrograph (DF-STEM) and selected area electron diffraction (SAED) patterns were obtained using the same instrument. Energy dispersive X-ray (EDX) analysis was performed on an INCA Energy TEM 200 using an X-ray detector. Fourier transform infrared (FTIR) spectra were recorded in the form of pressed KBr pallets in the range (400–4000 cm^{-1}) on a Shimadzu-FTIR Prestige-21 spectrophotometer. X-ray diffraction (XRD) pattern was obtained using a D8 ADVANCE BROKERaxs X-ray diffractometer with CuKα radiation ($\lambda = 1.5418$ Å); data were collected at a scan rate of 0.5° min^{-1} in the range of 10–80°. Electrochemical measurements were performed by a CHI-660C electrochemical workstation. A Ag/AgCl electrode (in 3.0 M KCl) and a Pt wire were used as the reference and auxiliary electrodes, respectively. Catalytic reactions were performed by the immobilized nanoparticles or nanocomposites over a 4-aminothiophenol monolayer modified gold working electrode, with 0.1 M phosphate buffer saline (pH ~ 7.5) used as the electrolyte and at a scan rate of 100 mV s^{-1}.

2.2. Synthesis of the nanomaterials

2.2.1 Synthesis of gold nanoparticles (NPs). Gold nanoparticles were synthesized by the Frens citrate reduction procedure,[35] where the standard procedure for the preparation

of 10 nm gold nanoparticles is as follows. An aliquot of 50 mL aqueous solution of $HAuCl_4 \cdot 3H_2O$ (0.25 mM) is heated to boiling and 0.5 mL of trisodium citrate (1%) is added. In about 25 s, the boiling solution turns faintly blue (nucleation). After approximately 70 s, the blue color suddenly changes into a brilliant red, indicating the formation of gold particles. The boiling was continued for half an hour and then cooled to room temperature.

2.2.2 Synthesis of gold–manganese oxide nanocomposites (NCs). Gold–manganese oxide nanoparticles were synthesised at the environmentally benign water/*n*-heptane interface under mild reflux conditions. In 25 mL binary solvent mixture of water and *n*-heptane (3 : 1 v/v), 2.5 mM $Mn(ac)_2 \cdot 4H_2O$ was added and brought to reflux (*ca.* 65–70 °C) under stirring. After about 30 min, 150 μL of ammonia was added, and immediately after, 1.0 mL of preformed gold nanoparticles (0.25 mM) was added dropwise for 10 min to the solution under reflux. The refluxing was continued overall for 1.5 h. After the addition of the gold colloid, the color of the sol slowly began to change, and finally, a brownish red coloration was seen at the end of the reaction. Then, the heating was stopped and the mixture was stirred for 12 h at room temperature. The particles obtained were retrieved from the solvent mixture by centrifugation at 10 000 rpm for 15 min and subsequently, redispersed into water. The dispersion was found to be stable for a month when stored in a vacuum desiccator. Manganese oxide nanoparticles were synthesised following the same procedure, but without the addition of any gold nanoparticles.

3. Results and discussion

In the present experiment, the water/*n*-heptane binary solvent mixture plays an important role in the evolution of gold–manganese oxide nanocomposites by epitaxial growth without any external stabilizing agents.[36] The controllable integration of gold and manganese oxide into single nanostructures was characterised by absorption, Fourier transform infrared (FTIR) spectroscopy and by X-ray diffraction (XRD) techniques, which revealed the epitaxial growth of manganese oxide on the surface of gold nanoparticles, as described in ESI 2.†

The morphology, composition and crystallinity of the particles are depicted in Fig. 1. Transmission electron micrographs (panels a, b and c) of gold, manganese oxide and gold–manganese oxide show that the particles are 10 ± 2 nm, 15 ± 3 nm and 20 ± 5 nm, respectively. In the image of the nanocomposites, the Au particles appear black, while Mn_3O_4 are light colored, because Au has a higher electron density and allows fewer electrons to transmit.[19] Dark field scanning tunneling electron micrographs (DF-STEM) (panel d) highlight the epitaxial growth of manganese oxide on gold nanoparticles. The energy dispersive X-ray spectrum (panel e) of Au–Mn_3O_4 particles reveals that the particles are composed of Mn, C, O, Cu and Au elements. Among these elements, the signals of Mn, O and Au result from the Mn_3O_4 and Au particles, which form the product and the signals of C, while the O and Cu elements come from the precursor and the supporting TEM grid. From the SAED pattern of the composites, it is clear that a bright reflection appears

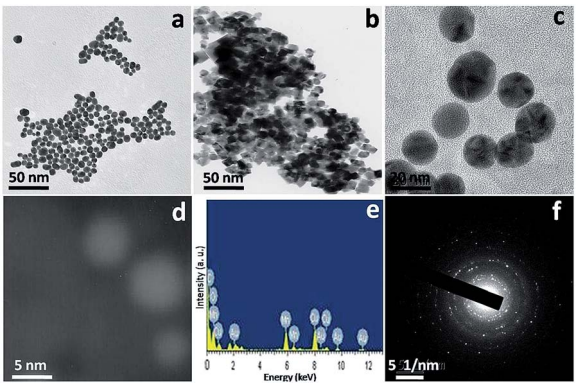

Fig. 1 (a–c) Transmission electron micrographs of Au, Mn_3O_4 and Au–Mn_3O_4 nanoparticles, respectively; (d) dark field scanning tunneling electron micrographs, (e) energy dispersive X-ray and (f) selected area electron diffraction pattern of Au.

from the (111) plane of the fcc-structured gold and the strong ring pattern corresponds to the (101), (103) and (211) planes of the tetragonal hausmannite structure. In addition, a combined multireflection results, due to the Au–Mn_3O_4 composite formation, confirming the crystallinity of the resultant materials.[19]

Nowadays, Au, Mn_3O_4 and Au–Mn_3O_4 nanoparticles are employed to investigate the electrocatalytic activity toward the water oxidation reaction. A detailed procedure of the modification of the electrodes is described in ESI 3.†

Fig. 2 displays the cyclic voltammogram of 4-ATP/gold (red), Au NPs/4-ATP/gold (green), Mn_3O_4 NPs/4-ATP/gold (blue) and Au–Mn_3O_4 NCs/4-ATP/gold (black) electrodes in PBS at pH ~ 7.5. A specific amount (20 μg) of the catalysts was dissolved in 10 mL of water in each case. These dispersions were then employed for the loading of catalysts by dipping the electrodes and allowing them to equilibrate overnight under vacuum. It was observed that the Au–Mn_3O_4 nanocomposites (black) caused a shift of the oxidation potential in the less

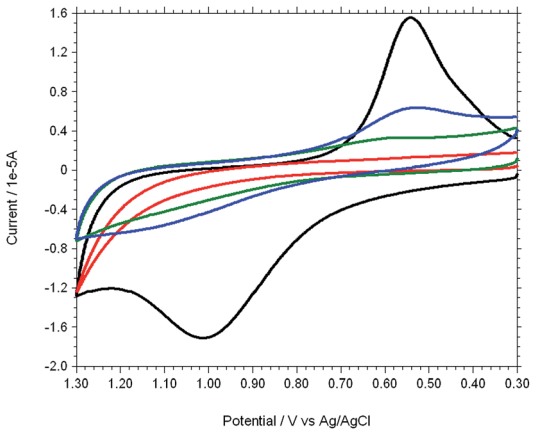

Fig. 2 Cyclic voltammograms of water oxidation in the presence of 4-ATP/gold (red), Au NPs/4-ATP/gold (green), Mn_3O_4 NPs/4-ATP/gold (blue) and Au–Mn_3O_4 NCs/4-ATP/gold (black) electrodes in PBS at pH ~ 7.5.

positive potential and a large increase in the current height compared to that of the only Au (green) or Mn_3O_4 nanoparticles (blue). In spite of the ideal electrocatalytic process at its thermodynamic potential (for example, at 0.62 V *vs.* Ag/AgCl, pH ~ 7.0 and 1 atm O_2), the actual electrode reaction occurs at a more positive potential (*i.e.* overpotential) whose magnitude reflects the electrode kinetics of the solution. It is seen that Au NPs/4-ATP/gold, Mn_3O_4 NPs/4-ATP/gold, and Au–Mn_3O_4 NCs/4-ATP/gold electrodes display an anodic response at +1.13 V ($\eta \approx 0.51$ V, pH ~ 7.5), +1.12 V ($\eta \approx 0.50$ V, pH ~ 7.5), and +0.998 V ($\eta \approx 0.37$ V, pH ~ 7.5) *vs.* Ag/AgCl, respectively, in the potential window of 0.3–1.3 V, signifying water oxidation in 0.1 M PBS (pH ~ 7.5) and a corresponding cathodic peak at ~+ 0.5 V for $O_2 + 4H^+ + 4e \rightarrow 2H_2O$ at pH ~ 7.5, which is indicative of the reversibility of the process,[3] whereas no such signal appears for 4-ATP/gold electrode. It was noted that the particles synthesized in the present experiment are stable for a couple of weeks without any significant agglomeration or precipitation of the particles. After the deposition of the particles at the electrodes, the catalytic activity of the particles was measured and the electrodes were rinsed in distilled water after the experiments. It was noted that the electrodes retained their catalytic activity even after 48 h of the loading of the catalysts. Therefore, it could be conceived that the particles do not suffer from dissolution or corrosion during the measurement of their electrocatalytic activity. However, assuming that the particles are nearly spherical and that the densities of Mn_3O_4 and Au–Mn_3O_4 are 4.86 and 12.09 g cm^{-3} (taking an average of the density of Au and Mn_3O_4) respectively, the number of Mn_3O_4 and Au–Mn_3O_4 particles is *ca.* 2.3×10^{12} and 3.8×10^{11}, respectively, and the corresponding surface areas are *ca.* 1625×10^{12} and 477×10^{12} nm^2, respectively.[37] Therefore, it is evident that Au–Mn_3O_4 composites are better electrocatalysts than Mn_3O_4 particles.

The turnover frequency (TOF) of the catalysts could be calculated using the equations:[38]

$$I_{cat} = nFAk_{cat}\Gamma_{cat} \quad (1)$$

$$\Gamma_{cat} = Q/nFA \quad (2)$$

where, I_{cat} is the catalytic current density, n is the moles of electron transfer, F is the Faraday constant, A is the geometric surface area of the underlying anodic surface, k_{cat} is the rate constant of the electron transfer, Γ is the surface coverage in moles per square centimeter, and Q is the charge obtained by integrating the cathodic peak ($= \int i_f dt$, where i_f is the Faradaic current). However, the concept of turnover frequency is based on the number of active sites of the catalysts. In the above equations, the active sites have been replaced by surface area, which is an apparent value; therefore, the calculated TOFs provide only apparent values rather than the real TOFs of the catalysts. In addition, for the catalyst of Au–Mn_3O_4, the active sites for Au are different from those for Mn_3O_4 and, as a result, the calculated TOF is a hybrid or average of that of the constituent particles. From eqn (1) and (2), we can estimate the electroactive site turnover rate during O_2 evolution as:

$$k_{cat} = I_{cat}/Q \quad (3)$$

The catalytic current densities for Au, Mn_3O_4, and Au–Mn_3O_4 are 3.8, 5.8 and 17.4 μA, respectively, and the charges obtained by integrating the cathodic peak for Au, Mn_3O_4, and Au–Mn_3O_4 is 2.4, 2.6, and 3.8 μC, respectively. Therefore, the turnover frequencies corresponding to Au, Mn_3O_4, and Au–Mn_3O_4 are *ca.* 1.6, 2.2, and 4.6 s^{-1}, respectively. The catalytic activity for water oxidation by Au–Mn_3O_4 nanocomposites is considered as not only combining the properties of both noble metal and metal oxides, but also the unique collective and synergistic effects of its component parts, compared to single component materials.[27,39]

Variation of the gold particle size in the nanocomposites shows that the catalytic activity increases with a decrease in the particle size of the nanocomposites (ESI 4†); this study elicits the reproducible electrocatalytic activity of the nanocomposites. Therefore, it could be conceived that Au–Mn_3O_4 composites are more efficient catalysts for the water oxidation reaction than the individual Au or Mn_3O_4 nanoparticles. The enhanced catalytic activity of the Au–Mn_3O_4 catalysts could be attributed to the beneficial presence of higher amounts of oxidizable gold species and surface oxygen vacancies, resulting from the strong interaction between Au and the reactive surface of Mn_3O_4 nanoparticles.[40] An increase in the 5d vacancy of Au increases the interaction of O_2 and Au, thereby, enhancing the catalytic activity of Au in the composites.[41] However, interestingly, it was noted while the electrode was cycled to the cathodic potential after several scans through the catalytic anodic wave, an irreversible peak was observed at *ca.* −0.001 V to −0.2 V for different modified electrode systems, as presented in Fig. 3. This peak could be attributed to the O_2/O_2^- couple[42] and indicates that O_2 evolved from water oxidation on the electrode surface. A digital camera photograph showing the evolution of oxygen gas during water oxidation and the corresponding cyclic voltammogram of the Au–Mn_3O_4 NCs/4-ATP/gold electrodes in normal and N_2-saturated PBS at pH ~ 7.5 is shown in ESI 5.†

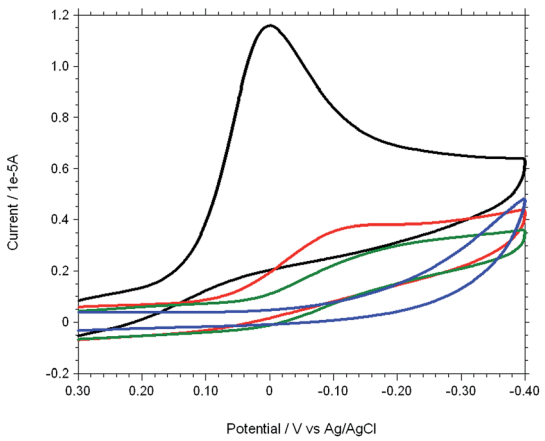

Fig. 3 Cyclic voltammograms for oxygen reduction in the presence of 4-ATP/gold (blue), Au NPs/4-ATP/gold (green), Mn_3O_4 NPs/4-ATP/gold (red) and Au–Mn_3O_4 NCs/ATP/gold (black) electrodes in PBS at pH ~ 7.5.

Under ambient conditions, the current height due to oxygen reduction is higher than in the N_2-sparged solution, which authenticates that the origin of this peak originated from O_2 reduction. In a likewise manner to water oxidation, the higher cathodic peak current and lower reduction potential with the Au–Mn_3O_4 NCs (black) electrode rather than with the Mn_3O_4 NP (red) and Au NPs (green)- modified gold electrodes authenticate that Au–Mn_3O_4 composites are better ORR catalysts than the individual Au or Mn_3O_4 particles.[37] The Au–Mn_3O_4 particles upon exposure to oxygen form radical species on the surface of the catalysts. The ability to form such radical species in the presence of oxygen leads to enhanced performance of the Au–Mn_3O_4 composites in the oxygen reduction reaction.[43] It is also likely that oxygen can dissociate on the Au surface and spill over from Au to the oxygen vacancies in the oxide, which synergistically promotes the adsorption and dissociation of O_2.[44] Therefore, the different surface structural features clearly determine the strength of the metal–support interaction and, thus, the catalytic activity. The overpotentials for Au, Mn_3O_4, and Au–Mn_3O_4 are 514, 505, and 370 mV, respectively. When Au interacts with transition metal oxides to form a reduced oxide and an oxidized metal at the interface of the two materials,[45,46] it dissolves at an oxidizing potential relevant to the water oxidation reaction.[47] Therefore, the presence of Au during the water oxidation reaction could lead to an enhancement in the electrocatalytic activity of Mn_3O_4 particles.

The oxidation of water to dioxygen is one of the key reactions that need to be fully understood for water splitting devices. A reasonable mechanism for the water oxidation and oxygen reduction reactions on the nanocomposite surface could be enunciated as follows. From an electrochemical perspective, this reaction can be divided into two half reactions, namely, water oxidation and proton reduction.[48] The formation of H_2O_2 from such species suggests that hydrolysis of an O–O bonded species proceeds more rapidly than the additional oxidation steps needed to form O_2. In the presence of the catalysts, an O–O bonded intermediate undergoes rapid electron transfer in the material or to the electrode to enable the selective evolution of O_2. In the present experiment, upon the addition of gold to the metal oxide system, the gold-metal oxide perimeter interface acts as a site for activating the reactants. Therefore, it could be conceived that the very strong metal–support interactions after Au deposition[49] create a unique interface, which results in enhanced activity for the water oxidation and oxygen reduction reactions.

Cyclic voltammetry data of water oxidation and oxygen reduction in the presence of the nanomaterials are summarized in Table 1. The overpotential of different manganese-based systems as a function of experimental conditions has been discussed elsewhere.[27] A comparative account of the pH conditions of the experiments and the overpotential of the Au–Mn_3O_4 composite and some other electrocatalysts is presented in ESI 6.†

Fig. 4 illustrates the cyclic voltammograms at varying pHs of the PBS with the Au–Mn_3O_4 NCs/4-ATP/Au electrode. A slight change of current height was observed for the O_2/O_2^- couple at −0.18 V, but the anodic peak potential, as well as the peak current, varying with the change in pH of the solution (Fig. 4A). A plot of potential *vs.* pH and the current *vs.* the pH (Fig. 4B) show that the potential is optimum at pH ∼ 7.5, and that the electrocatalytic activity for water oxidation increases with the increasing pH (5.5–9.5) of the solution, respectively.

In conclusion, the synthesis of stabiliser-free gold–manganese oxide nanocomposites by seed-mediated epitaxial growth, employing an environmentally benign water/*n*-heptane interface paves a facile strategy through surface attachment for combinatorial catalyst design. We have successfully overcome the key challenge in recent research of electrocatalytic water oxidation, surprisingly, at a nearly neutral pH (pH ∼ 7.5) and a low overpotential of 370 mV, which is beyond the typical range of many homogeneous water oxidation catalysts (600–900 mV). As manganese oxides are available in various oxidation states and exhibit extensive biomimetic chemistry with oxygen, this result adds a new feather and illuminates ample opportunities in water oxidation electrocatalysis using a wide variety of inexpensive and earth-abundant materials. This facile and

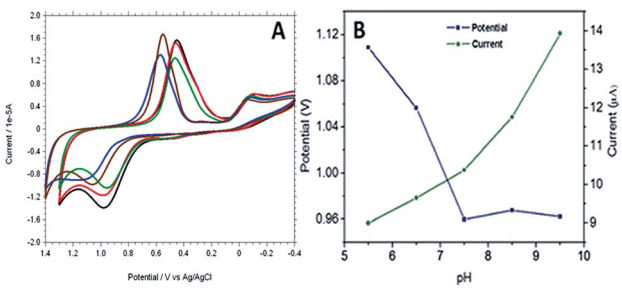

Fig. 4 (A) Cyclic voltammograms of water oxidation in 0.1 M PBS at pH ∼ 5.5 (blue), 6.5 (brown), 7.5 (green), 8.5 (red), and 9.5 (black) with Au–Mn_3O_4 modified electrodes; and (B) Profile showing the variation of current and potential as a function of pH.

Table 1 Cyclic voltammetry data of water oxidation and oxygen reduction in the presence of nanomaterials

Catalysts	Water oxidation potential ($E_{ox,\ H_2O}$), V	I_{pa}[a] (μA)	1st oxygen reduction potential ($E_{red,\ O_2}$), V	$I_{pc\ (1)}$[a] (μA)	2nd oxygen reduction potential ($E_{red,\ O_2}$), V	$I_{pc\ (2)}$[a] (μA)
Au	1.134	−4.5	0.562	3.3	−0.189	2.9
Mn_3O_4	1.125	−6.8	0.515	6.3	−0.139	3.8
Au-Mn_3O_4	0.998	−17.1	0.546	15.6	−0.001	11.6

[a] Where, I_{pa} and I_{pc} denote the irreversible peak currents at the anode and cathode, respectively.

environmentally benign synthetic strategy for nanocomposites could be upscaled to the industrial level and may offer a promising future for renewable energy technologies.

Acknowledgements

We gratefully acknowledge financial support from DST, New Delhi (Project no.:SR/FT/CS-68/2010).

References

1 J. K. Hurst, *Science*, 2010, **328**, 315–316.
2 S. Trassati, in *The Electrochemistry of Novel Materials*, ed. J.Lipkowski and P. N.Ross, Wiley VCH, 1994, ch. 5, pp. 207–296.
3 S. M. Barnett, K. I. Goldberg and J. M. Mayer, *Nat. Chem.*, 2012, **4**, 498–502.
4 R. Eisenberg and H. B. Gray, *Inorg. Chem.*, 2008, **47**, 1697–1699.
5 J. H. Alstrum-Acevedo, M. K. Brennaman and J. T. Meyer, *Inorg. Chem.*, 2005, **44**, 6802–6827.
6 F. Liu, J. J. Concepcion, J. W. Jurss, T. Cardolaccia, J. L. Templeton and J. T. Meyer, *Inorg. Chem.*, 2008, **47**, 1727–1752.
7 M. G. Walter, E. L. Warren, J. R. McKone, S. W. Boettcher, Q. Mi, E. A. Santori and N. S. Lewis, *Chem. Rev.*, 2010, **110**, 6443–6473.
8 N. S. Lewis, G. Crabtree, A. J. Nozik, M. R. Wasielewski and A. P. Alivisatos, *Basic Research Needs for Solar Energy Utilization*, Department of Energy, Washington, DC, 2005.
9 J. P. McEvoy and G. W. Brudvig, *Chem. Rev.*, 2006, **106**, 4455–4483.
10 M. Grätzel, *Acc. Chem. Res.*, 1981, **14**, 376–384.
11 N. S. Porter, H. Wu, Z. Quan and J. Fang, *Acc. Chem. Res.*, 2013, **46**, 1867–1877.
12 T. Nakagawa, N. S. Bjorge and R. W. Murray, *J. Am. Chem. Soc.*, 2009, **131**, 15578–15579.
13 L. Duan, F. Bozoglian, S. Mandal, B. Stewart, T. Privalov, A. Llobet and L. Sun, *Nat. Chem.*, 2012, **4**, 418–423.
14 M. J. Kenney, M. Gong, Y. Li, J. Z. Wu, J. Feng, M. Lanza and H. Dai, *Science*, 2013, **342**, 836–840.
15 J. Z. McAlpin, T. A. Stich, C. A. Ohlin, Y. Surendranath, D. G. Nocera, W. H. Casey and R. D. Britt, *J. Am. Chem. Soc.*, 2011, **133**, 15444–15452.
16 W. C. Ellis, N. D. McDaniel, S. Bernhard and T. J. Collins, *J. Am. Chem. Soc.*, 2010, **132**, 10990–10991.
17 S. M. Barnett, K. I. Goldberg and J. M. Mayer, *Nat. Chem.*, 2012, **4**, 498–502.
18 N. S. Lewis, *Science*, 2007, **315**, 798–801.
19 I. Djerdj, D. Arčon, Z. Jagličić and M. Niederberger, *J. Phys. Chem. C*, 2007, **111**, 3614–3623.
20 E. Grootendorst, Y. Verbeek and V. Ponce, *J. Catal.*, 1995, **157**, 706–712.
21 C.-C. Hu, Y.-T. Wu and K.-H. Chang, *Chem. Mater.*, 2008, **20**, 2890–2894.
22 S. K. Ghosh, J. Kang, M. Inokuchi and N. Toshima, *Appl. Catal., A*, 2014, **464–465**, 225–232.
23 M. Haruta, *Faraday Discuss.*, 2011, **152**, 11–32.
24 *Metal Nanoclusters in Catalysis and Materials Science: The Issue of Size Control*, ed. B. Corain, G. Schmid and N. Toshima, Elsevier, Amsterdam, 2008.
25 G. C. Dismukes, R. Brimblecombe, G. A. N. Felton, R. S. Pryadun, J. E. Sheats, L. Spiccia and G. F. Swiegers, *Acc. Chem. Res.*, 2009, **42**, 1935–1943.
26 Y. Gorlin and T. F. Jaramillo, *J. Am. Chem. Soc.*, 2010, **132**, 13612–13614.
27 Y. Gorlin, C.-J. Chung, J. D. Benck, D. Nordlund, L. Seitz, T.-C. Weng, D. Sokaras, B. M. Clemens and T. F. Jaramillo, *J. Am. Chem. Soc.*, 2013, **135**, 16977–16987.
28 M. M. Najafpour, A. N. Moghaddam, H. Dau and I. Zaharieva, *J. Am. Chem. Soc.*, 2014, **136**, 7245–7248.
29 M. Wiechen, I. Zaharieva, H. Dau and P. Kurz, *Chem. Sci.*, 2012, **3**, 2330–2339.
30 A. Singh, R. K. Hocking, S. L.-Y. Chang, B. M. George, M. Fehr, K. Lips, A. Schnegg and L. Spiccia, *Chem. Mater.*, 2013, **25**, 1098–1108.
31 M. Wiechen and L. Spiccia, *ChemCatChem*, 2014, **6**, 439–441.
32 M. Wiechen, M. M. Najafpour, S. I. Allakhverdiev and L. Spiccia, *Energy Environ. Sci.*, 2014, **7**, 2203–2212.
33 D. M. Robinson, Y. B. Go, M. Mui, G. Gardner, Z. Zhang, D. Mastrogiovanni, E. Garfunkel, J. Li, M. Greenblatt and G. C. Dismukes, *J. Am. Chem. Soc.*, 2013, **135**, 3494–3501.
34 A. Iyer, J. Del-Pilar, C. K. King'ondu, E. Kissel, H. F. Garces, H. Huang, A. M. El-Sawy, P. K. Dutta and S. L. Suib, *J. Phys. Chem. C*, 2012, **116**, 6474–6483.
35 G. Frens, *Nature*, 1973, **241**, 20–22.
36 M. Ali, S. K. Pal, H. Rahaman and S. K. Ghosh, *Soft Matter*, 2014, **10**, 2767–2774.
37 Y. Tang and W. Cheng, *Langmuir*, 2013, **29**, 3125–3132.
38 T. Nakagawa, C. A. Beasley and R. W. Murray, *J. Phys. Chem. C*, 2009, **113**, 12959–12961.
39 G. Li and Z. Tang, *Nanoscale*, 2014, **6**, 3995–4011.
40 F. W. Lytle, P. S. P. Wei, R. B. Greegor, G. H. Via and J. H. Sinfelt, *J. Chem. Phys.*, 1979, **70**, 4849–4855.
41 A. L. Ankudinov, J. J. Rehr, J. J. Low and S. R. Bare, *J. Chem. Phys.*, 2002, **116**, 1911–1919.
42 E. Yeager, *Electrochim. Acta*, 1984, **29**, 1527–1537.
43 M. M. Schubert, S. Hackenberg, A. C. van Veen, M. Muhler, V. Plzak and R. J. Behm, *J. Catal.*, 2001, **197**, 113–122.
44 L. M. Molina and B. Hammer, *Phys. Rev. Lett.*, 2003, **90**, 206102.
45 J. D. Benck, Z. Chen, L. Y. Kuritzky, A. J. Forman and T. F. Jaramillo, *ACS Catal.*, 2012, **2**, 1916–1923.
46 C. C. Chusuei and D. W. Goodman, in *Encyclopedia of Physical Science and Technology*, ed. A. M. Robert, Academic Press, New York, 3rd edn, 2003, pp. 921−938.
47 V. M.-W. Huang, V. Vivier, M. E. Orazem, N. Pébère and B. Tribollet, *J. Electrochem. Soc.*, 2007, **154**, C99–C107.
48 D. K. Zhong and D. R. Gamelin, *J. Am. Chem. Soc.*, 2010, **132**, 4202–4207.
49 C.-C. Hu, Y.-T. Wu and K.-H. Chang, *Chem. Mater.*, 2008, **20**, 2890–2894.